

UNIVERSITÀ DEGLI STUDI DI PAVIA

FACOLTÀ DI INGEGNERIA

Dipartimento di Ingegneria Civile e Architettura

**AORTIC ENDOGRAFTING:
RECONSTRUCTION OF STRUCTURAL
LOADING USING
COMPUTED TOMOGRAPHY**

Endograft aortico:

**Ricostruzione di carichi strutturali attraverso
l'utilizzo di tomografie computerizzate**

Supervisor:

PROF. FERDINANDO AURICCHIO

Co - supervisor:

DR. MICHELE CONTI

ING. MAURO FERRARO

Author:

GIULIA BORTOLOTTI

UIN 401638

Academic

year 2012/2013

*Alla mia mamma, al mio papà e alla mia sorellina. Grazie per avermi reso la persona che
sono.*

Ringraziamenti

Primo tra tutti ringrazio il prof. Ferdinando Auricchio per avermi dato questa opportunità di tesi e avermi sostenuto per tutta la durata del lavoro. Un ringraziamento particolare va al Dott. Michele Conti, per avermi supportato in tutte le varie fasi ostiche della tesi, e avermi regalato sempre una risata nei momenti più difficili. Grazie anche ai ragazzi del laboratorio, un gruppo fantastico umanamente e professionalmente, e soprattutto a Mauro, che mi ha aiutato a superare i momenti di 'non convergenza' più difficili. Ringrazio tutti i miei amici, per aver reso questi anni ingegneristici meno ostici e molto più vivibili; in particolare le mie amiche di vita, Dalila e Carlotta, per essermi sempre state accanto, nonostante i chilometri di distanza. Grazie a Silvia, amica di risate, di pianti e di serate indimenticabili. Ringrazio Elisa, Marco, Seba, Hilary, Ale per aver reso questi 'anni pavesi' meno difficili, facendomi sentire a casa. Grazie a tutta la mia famiglia siliquese e cagliaritana per essere sempre stata presente al mio rientro con pranzi, abbuffate, discussioni politiche e tanto amore. In particolare ringrazio i miei nonnini per avermi sempre sostenuto in tutti i modi possibili e immaginabili, soprattutto con i meravigliosi dolci di 'chez le negres' e le sebadas sempre presenti. Grazie a te nonna Giuliana, perchè se sono arrivata qui oggi, lo devo anche a te. Ultimo nell'elenco, ma primo nel mio cuore, ringrazio il mio ragazzo Maurizio per avermi sopportata giorno dopo giorno nei miei pochi (per fortuna sua) momenti no, per aver riso con me nei miei tanti momenti sì, e per rendermi giorno dopo giorno una persona migliore.

Abstract

The aorta is the main artery of the human circulatory system. The principal aortic diseases are aneurysms and dissections. The presence of these diseases can have a major impact on the entire body circulation. Traditionally vascular diseases are treated with surgeries called 'open surgery repair' (OSR). To overcome the high invasiveness of OSR, new techniques have been developed. The endovascular aortic repair (EVAR) is a new technology that allows to treat patients with aortic aneurysms through the insertion of a stent-graft and the subsequent isolation of the region affected by the disease. A stent is an expandable tube-like device that is inserted into a natural conduit of the body to restore a disease-induced localized stenosis or aneurysm. The EVAR is a treatment born for vascular diseases of abdominal aorta, but now the research field is trying to extend its use to other vascular regions (e.g, thoracic aorta and ascending aorta) but actually we do not have enough information about the treated problem. For this reason it is necessary to build and study few clinical cases analysed in the literature understanding the prosthesis performance. The encountered problems in the use of implants in these regions are mainly due to an adaptation of the device design, originally projected for other districts (e.g, stent implantation in the thoracic aorta with a design created for the abdominal aorta). In addition, for implanted stent-graft can occur a device malapposition in the aortic region, because they have to deal with anatomical reality much different with respect their mechanical simplification (e.g, modelled aorta mechanically as a 'straight pipe'). The available data for this study are relatively limited because, as already mentioned, it is a relatively new procedure and design associated with the implants are in constant change, while the clinical studies evaluate the effects of the stent at 6 months / 1 year. This aspect explains the parallel development of numerous aortic stent-graft, made with special materials, such as Nitinol, called *shape memory alloys* (SMA). It is necessary take into account several parameters to determine the optimal design of the stent. We focused to analyse stent regions most stressed by the pressure of the blood flow during the cardiac cycle, to prevent or improve the proper design and the mechanical characteristics of the stent in each patient.

In our study we focus on 74-year-old female, presented with an asymptomatic 5.5 cm pseudoaneurysm at the level of the distal anastomosis, 8 yr after ascending aortic repair for aneurysm.

IV

Endovascular exclusion of the pseudoaneurysm was planned, with the use of a custom-made stentgraft(Bolton Medical Inc., Sunrise,Florida,USA). From IRCCS San Donato Policlinic hospital(Milan), and in particular by the department of vascular surgery, we had access to the 4D CT scans of the patient, in order to compare the ideal model with clinical reality. To analyse the mechanical response of device we adopted a structural finite element analysis. Starting from its shape at rest, the stent is crimped (*crimping*) to be inserted within the catheter and once on site is partially released as a function of the artery diameter in which it is positioned. In this phase, known as *deployment* mechanical properties of the stent are calculated. After several operations analysis of CT images, which are necessary to extract the single ring from the TAC (*segmentation*) and to match the reference system of the model with the reference system of the implanted ring (*record*), we tried to deform the model of the stent, reproducing the deformation of the implanted stent. The analysis are implemented with Abaqus standard/explicit (Simulia Dessault Systems, Providence, RI, USA, v.6.12-1), which use finite element analysis. To reproduce the super-elastic material response for stent model, we adopted the Abaqus user material subroutine of the super-elastic model originally proposed by Auricchio and Taylor [11] [12]. By analysing the CT images we noted a strong correlation between the cardiac curve for an healthy patient and the configuration variation, in terms of distance, of the stent in different time instants. The variables analysed are the maximum values at specific regions of the stent, where there are bends and where you have the highest level of deformation. Despite a good overlap of the two models, there are regions that do not fit perfectly. The values found are comparable with the data available in the literature. This is a study with preliminary results that allow future analysis.

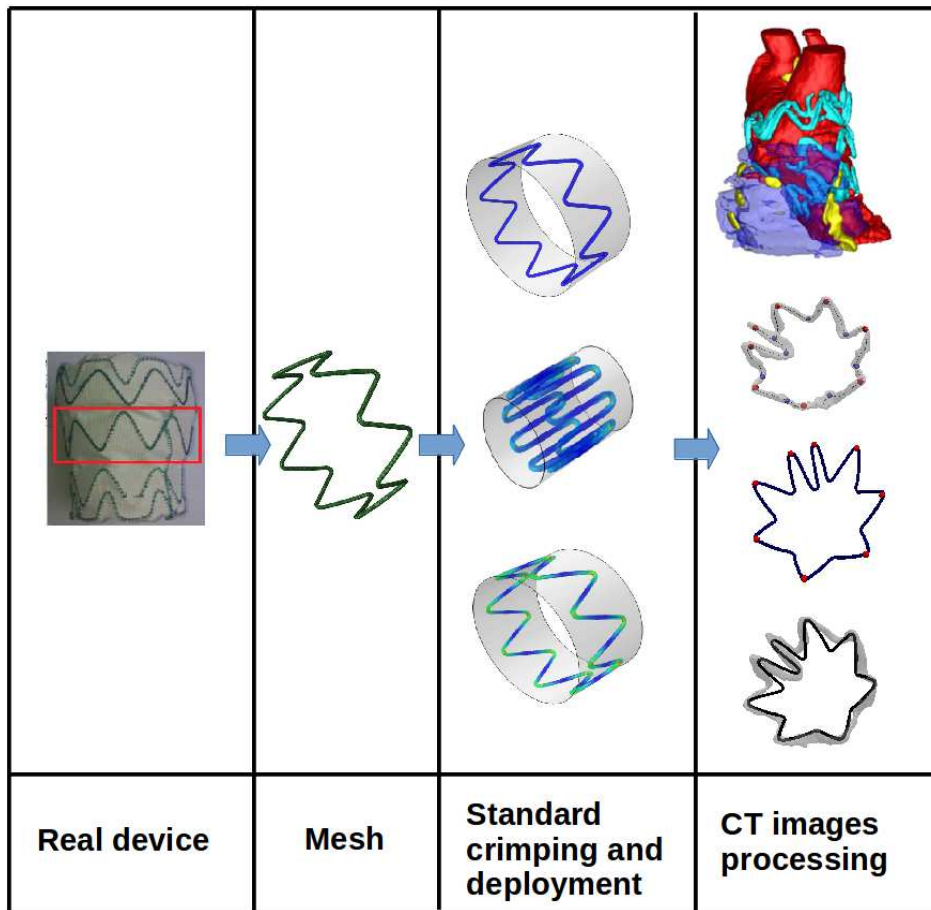


Figure 1: The image shows the workflow followed throughout the thesis. We started from the real device, which is then modelled in Abaqus. After we applied the analysis standard for the stress and strain calculation and we finished with the analysis of the CT images for the ideal case with the real case comparison.

Sommario

L'aorta è il principale vaso arterioso del sistema circolatorio umano. Le principali patologie legate all'aorta sono gli aneurismi, allargamenti non fisiologici della parete vascolare, e le dissezioni, dilaminazioni della tonaca del vaso con formazione di un secondo lume detto 'falso lume'. La presenza di queste patologie possono avere un impatto importante su tutta la circolazione.

Tradizionalmente le malattie endovascolari vengono trattate con operazioni chirurgiche, dette 'Open surgery repair', altamente invasive. Attualmente sono state sviluppate nuove tecniche per risolvere questo tipo di problematiche. Tra queste, il trattamento endovascolare miniminvasivo (EVAR) è una nuova tecnologia che consente di trattare pazienti con aneurismi aortici attraverso l'inserimento di stent-graft e il conseguente isolamento della regione interessata dalla patologia. Lo stent è una struttura metallica cilindrica a maglie che viene introdotta nei vasi sanguigni e viene fatta espandere fino a che il suo diametro è pari a quello del lume in modo da escludere l'aneurisma. L'EVAR è un trattamento nato per patologie vascolari dell'aorta addominale, ma attualmente si sta cercando di estendere il suo utilizzo anche in altre regioni vascolari, come l'aorta toracica e l'aorta ascendente. L'EVAR si basa, dunque, sull'uso di stent-graft che devono essere progettati per affrontare condizioni anatomiche e di sollecitazione ancora poco esplorate. Per questo motivo occorre basarsi e studiare i pochi casi clinici analizzati in letteratura e capire quali sono le sollecitazioni a cui va incontro la protesi. I problemi riscontrati nell'utilizzo delle protesi in queste regioni sono dovuti principalmente ad un adattamento del design del dispositivo, originariamente pensato per altri distretti (es. impianto nell'aorta toracica di uno stent con un design realizzato per l'aorta addominale). Inoltre gli stent-graft, una volta impiantati, non si appongono correttamente nella regione d'interesse, perchè devono affrontare delle realtà anatomiche ben lontane dalle loro semplificazioni meccaniche (es. aorta modellizzata meccanicamente come un 'tubo dritto'). I dati a disposizione per questo tipo di studio sono relativamente limitati perchè, come già detto, si tratta di una procedura relativamente recente e i design associati alle protesi sono in continuo cambiamento, mentre gli studi clinici valutano gli effetti degli stent a 6 mesi/1 anno. Da qui lo sviluppo parallelo di numerosi stent-graft aortici, realizzati con materiali partico-

lari, come il Nitinol, chiamati *a memoria di forma* (SMA). Si è reso necessario lavorare su diversi parametri che possono concorrere alla determinazione del design ottimale degli stent. Tra questi si è posto l'accento sull'andare ad analizzare le regioni dello stent maggiormente sollecitate dalla pressione del flusso sanguigno durante il ciclo cardiaco in modo da prevenire o migliorare il corretto design e le caratteristiche meccaniche dello stent in ciascun paziente. Il caso clinico analizzato nello specifico è quello di una donna di 74 anni con uno pseudoaneurisma asintomatico di 5.5 cm. La paziente è stata sottoposta ad un intervento minivasivo per escludere lo pseudoaneurisma con l'inserimento di uno stent realizzato su misura (Bolton Medical Inc., Sunrise, Florida, Usa). Dall'ospedale policlinico IRCCS San Donato (Milano), in particolare dal reparto di chirurgia vascolare, abbiamo avuto accesso alle tomografie computerizzate 4D della paziente, per poter confrontare il modello ideale con la realtà clinica. Durante lo sviluppo del modello si è cercato di riprodurre la dinamica a cui va normalmente incontro uno stent, attraverso l'utilizzo di un'analisi strutturale agli elementi finiti. Partendo dalla sua forma a riposo, lo stent viene crimpato (*crimping*) per essere inserito all'interno del catetere e una volta in loco viene parzialmente rilasciato in funzione del diametro dell'arteria in cui viene posizionato. In questa fase, detta di *deployment*, si sono calcolati i valori di stress di Von Mises e di strain associati allo stent. Le tomografie assiali computerizzate (TAC) del post-operatorio, a disposizione per lo studio, non presentano la possibilità di poter calcolare queste variabili, indispensabili per valutare e migliorare il design e i problemi precedentemente discussi degli stent. Nasce così la necessità di ricreare la situazione reale di azione ricostruendo il modello dello stent con le stesse condizioni di posizionamento e di deformazione della protesi impiantata nella paziente. Dopo diverse operazioni di analisi di immagini TAC, necessarie per poter estrarre il singolo ring dalla TAC (*segmentazione*) e per far coincidere il sistema di riferimento del modello con il sistema di riferimento del ring impiantato (*registrazione*), si è cercato di deformare il modello dello stent riproducendo la deformazione dello stent impiantato. Lo strumento attraverso il quale viene analizzato lo stent è il software ABAQUS (Simulia Dessault Systems, Providence, RI, USA, v.6.12-1), che sfrutta il metodo agli elementi finiti. Nello specifico per la modellizzazione del materiale dello stent viene utilizzata una particolare subroutine implementata in ABAQUS basata sul modello proposto da Auricchio e Taylor [11].

Analizzando le immagini TAC si è notata una forte correlazione tra l'andamento della curva sistolica di un paziente sano e la variazione, in termini di distanza, della configurazione dello stent nei diversi istanti temporali. Le variabili analizzate presentano i loro massimi valori in corrispondenza di specifiche regioni dello stent, ovvero in presenza di curvature e di un maggior livello di deformazione. Nonostante una buona sovrapposizione dello stent simulato, rispetto alle immagini TAC, si sono evidenziate delle regioni nelle quali la sovrapposizione non è perfetta. I valori trovati sono comparabili con la letteratura presente.

Contents

List of Tables	3
List of Figures	9
1 Introduction	11
1.1 Anatomical Point of view: aorta	11
1.2 Aortic diseases	13
1.2.1 Aneurysm	14
1.2.2 Dissection	14
1.3 Medical treatments	17
1.3.1 Open surgical repair	17
1.3.2 Endovascular aneurysm repair (EVAR)	18
1.3.3 Stent-graft finite element method overview	18
1.3.4 Thesis aim and organization	19
2 Shape memory alloys properties and numerical modelling	21
2.1 An introduction of shape memory alloys	21
2.2 SMA properties	22
2.2.1 Superelasticity, pseudoelasticity and SME	23
2.2.2 Kink resistance	25
2.2.3 Constant unloading stresses	25
2.2.4 Biocompatibility	26
2.2.5 Hysteresis	26
2.2.6 Fatigue resistance	27
2.3 Nitinol	27
2.3.1 Nitinol biomedical applications	28
2.4 Nitinol literature	34
2.5 Pelton 2013	35

2.6	Other References	36
3	Endograft Model Kinematics	41
3.1	Introduction	41
3.2	Finite element method (FEM)	42
3.2.1	Overview of the method	42
3.2.2	Abaqus software	43
3.2.3	Server information: cineca	45
3.3	Simulation strategy	46
3.3.1	Preprocessing: creating the model with Abaqus/CAE	47
3.3.2	Results	51
4	Medical imaging analysis and processing	55
4.1	Images set-up	55
4.2	Image segmentation	56
4.2.1	ITK-Snap software	57
4.3	CT images registration and centerline extraction	61
4.3.1	VMTK: The tool	62
4.4	Results	66
4.5	Endoprosthesis dynamics: real implanted device	66
5	Numerical Results	69
5.1	First approach: centerline analysis	69
5.1.1	Preliminary steps of work	69
5.1.2	Simulation strategy: from undeformed model to crimping and deployment state	72
5.1.3	Crimping: comparison between stress and strain values	72
5.1.4	Deployment: comparison between stress and strain values	74
5.2	Second approach: catheter analysis	76
5.2.1	Simulation strategy: from crimping to deformed state	76
5.2.2	Stress and logarithmic strain results	78
6	Conclusions	83
6.1	Limitations and future works	84
A	Iterative closest point algorithm (ICP)	87
	Bibliography	88

List of Tables

2.1	Sketch of the main NiTi applications in the biomedical field according to SMA properties.[27]	29
2.2	ABAQUS UMAT Parameters.	36
2.3	ABAQUS UMAT Parameters by different authors.	37
3.1	ABAQUS UMAT Parameters.	49
5.1	Error values.	71

List of Figures

1	The image shows the workflow followed throughout the thesis. We started from the real device, which is then modelled in Abaqus. After we applied the analysis standard for the stress and strain calculation and we finished with the analysis of the CT images for the the ideal case with the real case comparison.	V
1.1	Thoracoabdominal Aorta (Descending and Abdominal Aorta)	12
1.2	(a) Abdominal aortic aneurysms (AAA). (b) Thoracic aortic aneurysms (TAA). (c) Thoracoabdominal aortic aneurysms.	15
1.3	Aortic layers : Intima, media, adventitia	15
1.4	Comparison between healty aorta and different type of dissections	16
1.5	Open Aortic Aneurysm Repair	17
1.6	Endovascular aortic repair (EVAR)	18
2.1	Stress-strain curves for a specimen in Austenitic Phase, with a temperature between A_f and M_d . Within this range of temperature, also for martensitic transformation stress-induced, the material presents a pseudoelastic (right) or superelastic (left) behavior.	23
2.2	Two-dimensional schematization of the phase transformation from austenite to martensite, where a) is fully austenite and d) fully martensite. As shown in c), the atomic displacement occurs over short distances, such as not involve the breaking of chemical bonds.	24
2.3	Thermomechanical cycle in a diagram load-strain-temperature representative of the memory one way effect.	25
2.4	A schematic model of martensitic transformation.	26
2.5	Comparison between the stress-strain diagram of Nitinol (in red) and that of steel (in blue).	27
2.6	SMA orthodontic wires.	30
2.7	SMA orthodontic distracters. [27]	30

2.8	Fig.(a) NiTi plate for mandible fracture, Fig.(b) spinal vertebrae spacer. [27]	31
2.9	Fig.(a) Venous filter: Simon filter, Fig.(b) Example of SMA stents: (top right) coronary stent, (top left) carotid stent, (bottom left) femoral stent [27].	33
2.10	Example of stent-graft in NiTi alloys.[7]	33
2.11	CoreValve aortic valve http://www.medtronic.com/corevalve/ous/index.html . . .	34
2.12	NiTi self-expandable neurosurgical stent (Enterprise Vascular Reconstruction Device; Cordis Corp., Miami Lakes, FL) [27].	34
2.13	cube subjected to tension-compression uniaxial test in x direction	35
2.14	Pelton Review. Compare Nitinol behaviour for $T=22^\circ$, $T=37^\circ$ and $T=60^\circ$. . .	37
2.15	Nitinol material properties (from ABAQUS Nitinol UMAT). Nitinol parameters based on the uni-axial behaviour (from ABAQUS Nitinol UMAT)) where E_A Austenite elasticity, ν_A Austenite Poisson's ratio, E_M Martensite elasticity, ν_M Martensite Poisson's ratio, ϵ_L^L Transformation strain, $(\delta\sigma/\delta T)_L$ loading, σ_L^S Start of transformation loading, σ_L^E End of transformation loading, T_0 Reference Temperature, $(\delta\sigma/\delta T)_U$ unloading, σ_U^S Start of transformation unloading, σ_U^E End of transformation unloading, $\sigma_C L^S$ Start of transformation stress during loading compression as a positive value, ϵ_V^L Volumetric transformation strain, N_A Number of annealing to be performed during the analysis. [6]	38
2.16	Compare Nitinol behaviour for $T=37^\circ$ by different authors.	39
3.1	Qualitative comparison between implicit and explicit methods in terms of computational cost.	43
3.2	Abaqus interface	44
3.3	Abaqus analysis flow.	46
3.4	Cylindric surface representation used for the catheter model.	46
3.5	Fig.(a): Real device. Fig.(b): Final finite element model (only central ring). . .	47
3.6	Planar stent (left) and 3D stent (right) representation.	48
3.7	Crimping analysis steps (left to right). Stress values are calculated for maximum crimping state.	52
3.8	Deployment analysis steps(left to right). Stress values are calculated for maximum deployment state.	53
3.9	Histogram of von mises stress distribution during crimping step and deployment step, compared to number of elements which have those stress values in 8 characteristic integration points for each element. The stress values are plotted as the mean for each integration point and are calculated in MPa units. The number of elements are normalised respect with maximum number of elements.	53

3.10	Crimping analysis steps (left to right) with logarithmic strain values.	54
3.11	Deployment analysis steps with logarithmic strain values.	54
3.12	Histogram of logarithmic max. principal strain distribution during crimping step and deployment step, compared to number of elements which have those strain values in 8 characteristic integration points for each element. The strain values are plotted as the mean for each integration point and are calculated in MPa units. The number of elements are normalised respect with maximum number of elements.	54
4.1	ITK Snap software interface. Viewing of segmented TAC images. In the window in the lower left Endograft volume rendering.	58
4.2	ROI definition for endograft segmentation.	59
4.3	<i>Pre-processing</i> of the image based on the <i>intensity regions</i>	59
4.4	Arrangement of seed within the area to be segmented.	60
4.5	Segmentation results.	61
4.6	Extraction of stent central ring from image segmented.	61
4.7	Result of ICP registration between the undeformed model (white) and CT image (blue).	63
4.8	VMTK centerline reconstruction.	64
4.9	Clip filter applied to the ring using Paraview.	65
4.10	Opened structure after Paraview manipulation	65
4.11	In this graphic we compare the distance between first frame and the others from CT images with characteristic systolic curve (the first frame with the second, the first with the third frame and so on) to see if there is a correlation between the two curves. The x axis represent the normalised time and y axis has normalised pressure from a characteristic systolic curve in healthy patient, compared to normalised distance of the stent during different frames.	66
4.12	In this graphic we compare the distance between frames couples from CT images (the first frame with the second, the second with the third and so on) to see if there is a particular trend. The x axis represent the normalised time and y axis represents the distance of the configurations of the stent in different time instants.	67
5.1	ABAQUS. Central nodes of stent	70

5.2	ABAQUS. von Mises stress calculated by applying a deformation analysis at initial configuration of stent(a) and by applying BCs of central nodes(b). The stress values represent the interval values assumed by the model during the analysis.	70
5.3	ABAQUS. Displacement calculated by applying a deformation analysis at initial configuration of stent (a) and by applying BCs of central nodes (b). The displacement values represent the interval values assumed by the model during the analysis.	71
5.4	Planar stent, 3D stent representation and central nodes set of 3D stent configuration.	72
5.5	Crimping and deployment analysis steps by applying Boundary conditions to wire centerline (left to right, up to down). The stress values represent the interval values assumed by the model during the analysis.	73
5.6	Von Mises stress values during crimping analysis with two approaches.	73
5.7	Logarithmic strain values during crimping analysis with two approaches.	74
5.8	Von Mises stress values during deployment analysis with two approaches.	74
5.9	Logarithmic strain values during deployment analysis with two approaches.	75
5.10	Von mises stress distribution in catheter analysis (left) and centerline analysis (right).	75
5.11	from left to right. Rigid surfaces used for contact analysis to deform the stent from undeformed configuration (a) to crimping configuration (b) and from crimping configuration to first CT image configuration (c).	77
5.12	CT image considered for the deformation analysis of the stent. Upper nodes (red) and lower nodes (black) are highlighted. The lower nodes are blocked along theta cylindrical coordinate to avoid rotations, and to upper nodes we imposed, as boundary conditions, coordinates values from upper nodes of this frame.	78
5.13	Crimping step and deformation step. Comparison between modelled stent and real implanted device. The arrows in the left image indicate how we moved the nodes of interest to go from the crimped configuration, the deformed configuration.	78
5.14	The image represents the distribution of the distance into the stent simulated, compared to the implanted stent after the analysis of contact. The highest values of distances are at the nodes more deformed stent, as expected. The distance is calculated in millimetre.	79
5.15	Von mises values calculated during the analysis. The stent figure is referred to the last frame of the second step. The values are calculated in MPa.	79

- 5.16 Logarithmic max principal strain calculated during the analysis. The stent figure is referred to the last frame of the second step. The values are calculated in millimetres. The red rectangle highlights the regions with a high value of deformation in the stent. 80
- 5.17 Histogram of von mises stress distribution during crimping step and deployment step, compared to number of elements which have those stress values in 8 characteristic integration points for each element. The stress values are plotted as the mean for each integration point and are calculated in MPa units. The number of elements are normalised respect with maximum number of elements. 80
- 5.18 Histogram of logarithmic max. principal strain distribution during crimping step and deployment step, compared to number of elements which have those strain values in 8 characteristic integration points for each element. The strain values are plotted as the mean for each integration point and are calculated in MPa units. The number of elements are normalised respect with maximum number of elements. 81

Chapter 1

Introduction

Endovascular treatment of the aorta by stent-grafting is receiving more and more attention, since it is a promising method, less invasive than the alternative of traditional surgical repair. From the introduction in the clinical field in 1990, the aortic endografts were used for exclusion of abdominal aortic aneurysms. These endografts have been used increasingly for treatment of aneurysms, dissections, and traumatic ruptures of the aorta with good results in the short and medium term. Both pathological conditions can be treated using the endovascular technique. This method is more convincing by the fact that the classic surgical treatment often involves high pre-operative mortality, with serious complications. In this context, the integration of clinical considerations with dedicated bioengineering analysis, combining the vascular features and the prosthesis design, might be helpful to plan the procedure and predict its outcome. Starting from a brief anatomy introduction of aorta, aortic diseases and different medical treatments will be described. At the end of the chapter, the aim and the structure of this thesis will be detailed.

1.1 Anatomical Point of view: aorta

The aorta, figure 1.1, is the largest artery in the human body, originating from left ventricle of the heart and extending down to the abdomen, where it bifurcates into two smaller arteries (the common iliac arteries). The aorta distributes oxygenated blood to all parts of the body through the systemic circulation. The size of the aorta is directly proportionate to the patient's height and weight. Its diameter may range from 3 cm (more than an inch) to 1.2 cm (half an inch). It is typically the largest in the aortic root and smallest in the abdominal aorta. In anatomical sources, the aorta is usually divided into seven sections [13].

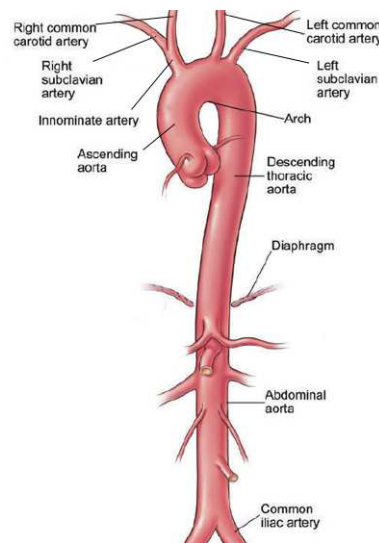


Figure 1.1: Thoracoabdominal Aorta (Descending and Abdominal Aorta)

Aortic valve

The aorta starts with the aortic valve just below the first branches of the aorta, the coronary arteries. It is the most important valve of the heart and the most commonly replaced heart valve. The aortic valve usually has three leaflets and commissures (tricuspid) but may also have two leaflets and commissures (bicuspid aortic valve). The patient with bicuspid aortic valve have a much higher chance to develop aneurysms and dissection (splitting or separating of tissues) of the aortic root and the ascending aorta.

Aortic root

The aortic root is the segment above the aortic valve and below the sinotubular junction. The left and right coronary arteries - supplying the heart with oxygenated blood – arise here from the sinuses of Valsalva. Aortic root is typically aneurysmal in many patients with connective tissue disorder.

Ascending aorta

The ascending aorta is the segment between the sinotubular junction and the largest aortic branch vessel; the innominate (brachiocephalic) artery. This is the only portion of the aorta that does not give any branch vessels. The ascending aorta is the most anterior (toward the front of the body) portion of the aorta. Therefore, the most common symptom from the ascending aorta and the aortic root is chest pain. This pain may be confused with chest pain associated with ischemic heart disease (coronary artery disease).

Aortic arch

The aortic arch (transverse aorta) is a short segment where branch vessels to the head and arms start. It has typically three branches: first, the innominate (brachiocephalic) artery supplies right arm and right portion of head and brain with oxygenated blood. Next, the left carotid artery carries blood to the left head and brain. The last branch vessel from the aortic arch is usually the left subclavian artery supplying the left arm with blood. There are many anomalies of the aortic arch such as the bovine arch, where there are only two branch vessels off the aortic arch. The operations involving the aortic arch usually require the body to be cooled down using the heart-lung machine. This technique is called hypothermic circulatory arrest. Alternatives are complex hybrid operations that usually do not require heart-lung-machine.

Descending thoracic aorta

The descending thoracic aorta starts with the last branch vessel off the aortic arch and ends at the first branch in the abdominal aorta; the celiac artery. The descending thoracic aorta is the most posterior (toward the back of the body) portion of the aorta. Therefore, the most common symptom from the descending thoracic aorta is back pain, and it may be confused with back pain associated with back muscles, joints and nerve pain. The descending thoracic aorta has many branches that supply a portion of the spinal cord (the out-pouching of brain within the spinal column). Therefore, any intervention involving this portion of the aorta has the risk of spinal cord ischemic injury.

Abdominal aorta

The abdominal aorta branches to the intestine and the kidneys and divides into left and right common iliac arteries. The branch vessels of the abdominal aorta include the celiac artery, the superior mesenteric artery, the left and right renal arteries, and the inferior mesenteric artery.

Thoracoabdominal aorta

The Thoracoabdominal aorta is the segment starting past the last branch of the aortic arch and ends with the abdominal aortic bifurcation into left and right common iliac artery.

1.2 Aortic diseases

Diseased aortic tissue is characterized by degeneration of the cells composing the aortic wall. This diseased tissue is weak, lacking sufficient elastic components to stretch and contract well.

The first indication of this abnormality may be a localized enlargement in the area of weakness. When it reaches a certain size this enlarged area is referred to as an aneurysm. Aortic tissue may also tear, even if the aorta is not enlarged. Tearing of the inner layer of the vessel wall allows blood to leak into the middle layer of the aorta, separating the inner and outer layers. This is called dissection.

1.2.1 Aneurysm

Three types of aortic aneurysms can be classified as:

Abdominal aortic aneurysm

An abdominal aortic aneurysm, figure 1.2.1 (a), is an enlarged area in the lower part of the aorta, the major blood vessel that supplies blood to the body. The aorta, about the thickness of a garden hose, runs from your heart through the centre of your chest and abdomen. Because the aorta is the body's main supplier of blood, a ruptured abdominal aortic aneurysm can cause life-threatening bleeding.

Thoracic aortic aneurysm

An aortic aneurysm, figure 1.2.1 (b), is an enlargement of a weakened area of the aorta. Aneurysms which involve the ascending aorta, aortic arch and descending thoracic aorta are termed "thoracic aortic aneurysms." Aneurysms in these regions are prone to rupture once they reach a certain size (see below). Fifty percent of patients who experience a rupture of a thoracic aortic aneurysm die before reaching the hospital. Furthermore, surgical repair of a ruptured thoracic aneurysm carries a 25-50% mortality as opposed to a 5-8% mortality when such aneurysms are treated electively.

Thoracoabdominal aortic aneurysm

Thoracoabdominal aortic aneurysms, figure 1.2.1 (c), result from continuous dilation of the descending thoracic aorta extending into the abdominal aorta.

1.2.2 Dissection

The aorta has many layers, as we can see in figure 1.3 .

- The intima, the innermost layer, provides a smooth surface for blood to flow across.
- The media, the middle layer with muscle and elastic fibers, allows the aorta to expand and contract with each heartbeat.

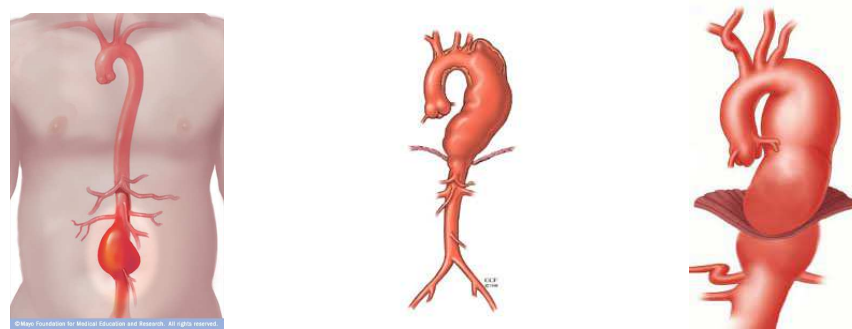


Figure 1.2: (a) Abdominal aortic aneurysms (AAA). (b) Thoracic aortic aneurysms (TAA). (c) Thoracoabdominal aortic aneurysms.

- The adventitia, the outer layer, provides additional support and structure to the aorta.

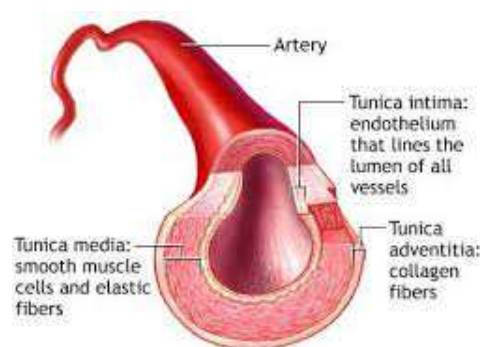


Figure 1.3: Aortic layers : Intima, media, adventitia

Aortic dissection, figure 1.4, is a tear that develops in the inner layer of the aorta, causing blood to flow between the layers. The layers then separate, interrupting the blood flow and possibly causing the arterial wall to burst. Aortic dissection can be a life-threatening emergency, in some situations requiring emergency surgery to repair or replace the damaged segment of the aorta.

Type A

Type A aortic dissections are the more common and dangerous type of aortic dissection. These dissections involve a tear in the ascending portion of the aorta just where it exits the heart or a tear extending from the ascending portion down to the descending portion of the aorta, which may extend into the abdomen.

Type B

This type of aortic dissection involves a tear in the descending aorta only, which may also extend into the abdomen.

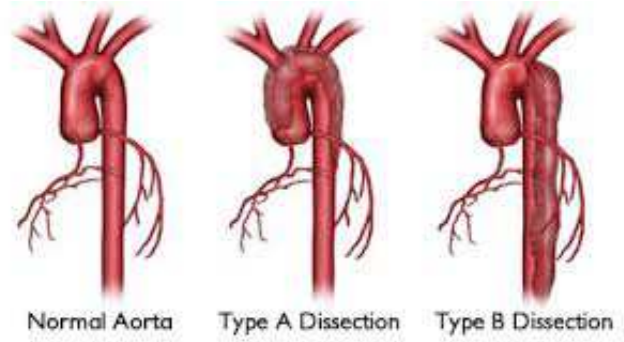


Figure 1.4: Comparison between healthy aorta and different type of dissections

1.3 Medical treatments

1.3.1 Open surgical repair

The decision to treat an aneurysm with surgery is determined by many factors, including:

- The presence of symptoms, including chest and back pain, and pain in the jaw, neck and upper back;
- if the aneurysm is growing more than 1 centimetre (cm) for year;
- signs of an aortic dissection, including sudden, severe sharp tearing pain in the chest or back;
- the age of the patient and the patient's overall medical condition.

New evidence has shown that the size of the aneurysm in addition to a patient's height plays an important role in the decision for surgery. The current standard surgical treatment of an aortic aneurysm is the open-chest approach, as shown in figure 1.5. The main purpose of open-chest surgery to treat a thoracic aneurysm is to replace the weakened portion of the aorta with a fabric tube, called a graft. Repairing an aortic aneurysm is surgically complicated and requires an experienced surgical team. However, neglecting the aneurysm presents a higher risk.

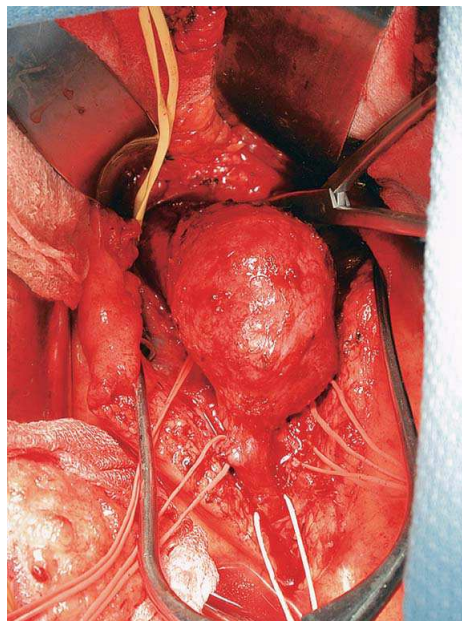


Figure 1.5: Open Aortic Aneurysm Repair

1.3.2 Endovascular aneurysm repair (EVAR)

A new procedure called Endovascular repair of aneurysms has been developed over the last twenty years, figure 1.6. Endovascular means that surgery is performed inside the aorta using thin, long tubes called catheters. Through small incisions in the groin, the catheters are used to guide and deliver a stent-graft (SG) through the blood vessels to the site of the aneurysm. This technique consists in excluding the aneurysm sac from the main stream circulation by the Endovascular insertion of a SG via the femoral arteries. An endovascular stent graft is a fabric tube supported by metal wire stents (also called a scaffold) that reinforces the weak spot in the aorta. By sealing the area tightly with your artery above and below the aortic aneurysm, the graft allows blood to pass through it without pushing on the aneurysm. Endovascular repair of aortic aneurysms is generally less painful and has a lower risk of complications than traditional surgery because the incisions are smaller. Besides EVAR is associated with lower post-operative morbidity and mortality compared with the invasive traditional surgical procedure to treat aneurysms. Endovascular aorta aneurysm procedures also allow to leave the hospital sooner and recover more quickly after your aorta repair. However, SG durability remains the principal issue.



Figure 1.6: Endovascular aortic repair (EVAR)

1.3.3 Stent-graft finite element method overview

The use of finite element analysis in stent-graft simulation is proposed by several papers in literature. For example Petrini et al. [19], use the finite element method to understand the effects of different geometrical parameters (thickness, metal-to-artery surface ratio, longitudinal and radial cut lengths) of a typical diamond-shaped coronary stent on the device mechanical

performance, to compare the response of different actual stent models when loaded by internal pressure and to collect suggestions for optimizing the device shape and performance. Pelton et al. [28] studies Nitinol stent-graft performance in different Nitinol materials. Kleinstreuer et al. [6] analyse the effects of crimping, deployment, and cyclic pressure loading on stent-graft fatigue life, radial force, and wall compliances for different types of realistic stent-grafts. Debock et al. [25] present a study, detailing the virtual deployment of a bifurcated stent-graft in a abdominal aortic aneurysm model, using finite element method. In particular Auricchio et al. [10, 12] in the first article try to evaluate the performance of three self-expanding stent designs in carotid artery and the second article describe the use of a custom-made stent-graft to perform a fully endovascular repair in a patient with finite element method. There are many informations in literature about use in biomedical research of aortic stent-graft. Starting from those information we develop our study and describe thesis organisation.

1.3.4 Thesis aim and organization

After a brief introduction that highlights the anatomical location of the problem, the thesis develops focusing on aortic endografts which are used in minimally invasive surgery to minimize the rupture risk of different types of aneurysms. To achieve the endograft, materials with peculiar mechanical properties are used. Despite of the great commercial interest in this topic, there is still the strong need of investigation tools, focused on the optimization of devices design. These tools, based on engineering methods, have to predict the behaviour of the devices taking into account the material properties. As seen previously in 1.3.2, the aortic endograft is positioned in loco by using catheters. By developing an endograft model, using finite element analysis (FEA), is possible to predict and calculate stress and strain values in the device after surgery, to evaluate which are the most stressed points that could lead to a new surgery for the patient. The aim of this thesis is to develop an endograft model that reproduces the same conditions of implantation and positioning obtained by devices actually implanted. This is made by using post-operative CT images, useful for the model realisation. Finite elements analysis (FEA), result a valid tool to evaluate the design of devices and to predict the material performance. In particular, Abaqus, one of the most used FEA commercial solver, is used. The thesis is structured as follows:

- **Chapter 2:** this chapter is focused on the description of shape memory alloys (SMA) behaviour. Starting from the role of innovative materials in the technological progress, SMA discovery and evolution will be described. In order to briefly explain the reasons of the great success of SMA, their physical properties will be detailed. After that, a quick overview of SMA application fields and literature references of Nitinol use for aortic

stent-graft modelling will be discussed.

- **Chapter 3:** endograft model development will be detailed, with particular care to used materials and method and FEA settings. In this chapter we start studying the ring kinematics trough catheter which represent the standard method used for idealising stent-graft simulation.
- **Chapter 4:** in this chapter we focus on medical imaging analysis and processing based on segmentation, registration and wire centerline ring extraction. The mail goal is to have comparable situation between ring model simulation and CT images from patient.
- **Chapter 5:** the study ends with results obtained from the analysis. To evaluate stent kinematics comparing post-precessed CT images, we develop a method that exploits the use of a rigid surface (catether) to induce the deformation characteristics of the implanted device, starting from the undeformed model realized in Abaqus. We propose a second approach that allows to define stresses imposed on the stent during crimping and deployment state through boundary conditions applied to the central nodes of the undeformed model. Preliminary results are discussed.

Chapter 2

Shape memory alloys properties and numerical modelling

This chapter describes the behaviour of shape memory alloys (SMA). Starting from the role of innovative materials in the technological progress, SMA discovery and evolution will be described. In order to briefly explain the reasons of the great success of SMA, their physical and mechanical properties will be detailed with particular attention to pseudo elasticity and shape memory effect.

2.1 An introduction of shape memory alloys

Shape memory alloys are special metal materials that have exclusive properties, two in particular: the capability to remember a specific geometric macroscopic shape impressed by special thermomechanical treatments, a phenomenon called Shape Memory Effect (SME), and the possibility of a 10% deformations, retrieving them completely during the unloading phase, without evidence of plasticity phenomena, properties known to Superelasticity (SE). Both of these properties are due to a transition of thermoelastic martensitic phase, which can be or induced by a temperature change or by a state of stress agent on the material. In fact, depending on the temperature and imprinted stress, such materials may present two different crystallographic phases, said austenitic phase and martensitic phase: the transformation of the one into the other are responsible of the properties previously mentioned. The first to discover the transformation associated with the shape memory alloy in a metal were two researchers, Chang and Read in 1932. They noted the reversibility of the martensitic transformation in an alloy based on AuCd metallographic observations and variation in resistivity of the material [16]. Subsequently, a similar behavior was observed in 1938 in a CuZn alloy (brass) at the Massachusetts Institute of Technology, but the official shape memory alloys

recognition took place only thirty years later, in 1962, when Buehler [9] and his collaborators at the laboratories of the NOL (U.S. Naval Ordnance Laboratory) accidentally discovered the shape memory alloy NiTi-based system while they were working on a project on a material resistant to corrosion and high temperatures. Since then began the first studies on this class of materials and, in particular, on the Nitinol (an acronym of nickel, titanium and NOL). In the following decades shape memory alloys became the subject of considerable scientific and commercial interests, so that a large number of products, based on these materials, were used in mechanical and chemical engineering, medicine and other several activities. Since the 80's, these materials have been investigated deeper for macroscopic properties to understanding their complex transformation mechanism (martensitic transformation). Thanks to their lower cost compared to NiTi alloys, recently copper-based alloys, such as ternary alloys CuZnAl and CuAlNi, were developed. The properties of these materials are very different from each other: the NiTi alloys, for example, have a higher deformation for the shape memory effect of the (up to 10% compared with 5% of copper based alloy), are more thermally stable, have excellent resistance to corrosion and stress corrosion. Moreover, the greater mechanical strength allows the use for the realization of mechanical joints and sealing, and the corrosion resistance, as well as the biocompatibility, such that these can be used in the biomedical field. The best properties of NiTi alloys have meant that these remained, however, the most studied and applied.

2.2 SMA properties

The main SMA properties are:

- Pseudoelasticity (PE): capability to recover strains after stress-induced large deformations;
- Shape memory effect (SME): capability to recover plastic strains after an heating process;

These principal properties are linked with other important properties:

- Kink Resistance;
- Constant Unloading Stresses;
- Biocompatibility;
- Hysteresis;
- Fatigue Resistance.

2.2.1 Superelasticity, pseudoelasticity and SME

One of the most important SMA properties is the superelasticity phenomenon: the object considered is subjected to large deformations (up to about 10% of its original length), within a characteristic temperature range, and it recovers them. When the deformation recovery follows a linear stress-strain diagram, the right term is pseudoelasticity (Fig.2.1 on the right), while, if the recovery follows a non-linear diagram, the phenomenon is called superelasticity (2.1 on the left).

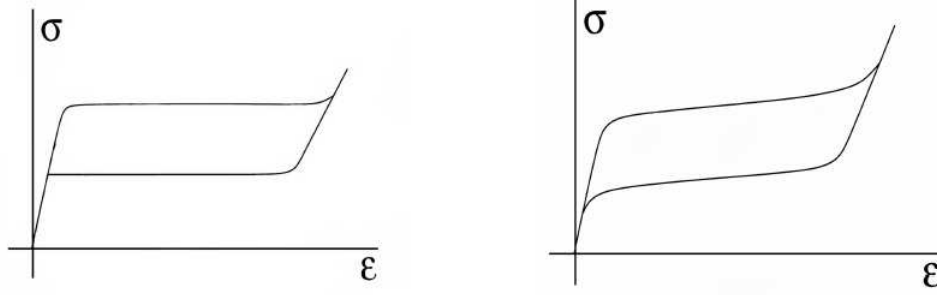


Figure 2.1: Stress-strain curves for a specimen in Austenitic Phase, with a temperature between A_f and M_d . Within this range of temperature, also for martensitic transformation stress-induced, the material presents a pseudoelastic (right) or superelastic (left) behavior.

Both PE and SME effects are strongly related to the martensitic transformation (MT). This phenomenon is a diffusionless phase transformation in solids, in which atoms move cooperatively, often by shear-like mechanism. The transformation from one structure to the other one does not occur by diffusion of atoms, but by shear lattice distortion. This particular phenomenon is associated with the crystallographic organization of SMA, characterized by a two-solid phases structure:

- Austenitic phase: characterized by an high symmetric crystallographic structure. This phase is stable at high temperatures ($T > A_f$, austenite finish transformation temperature).
- Martensite phase: stable at temperatures $T < M_f$, with M_f finish transformation temperature. This phase presents a low symmetry structure.

As shown in figure 2.2 the progress of transformation inside the material in the transition from austenite to martensite occurs along an interface that affects a single plane of atoms at a time. To each individual atom is required a movement such as not to generate the breaking of chemical bond. As shown in figure 2.3, in the origin of the diagram is the martensite

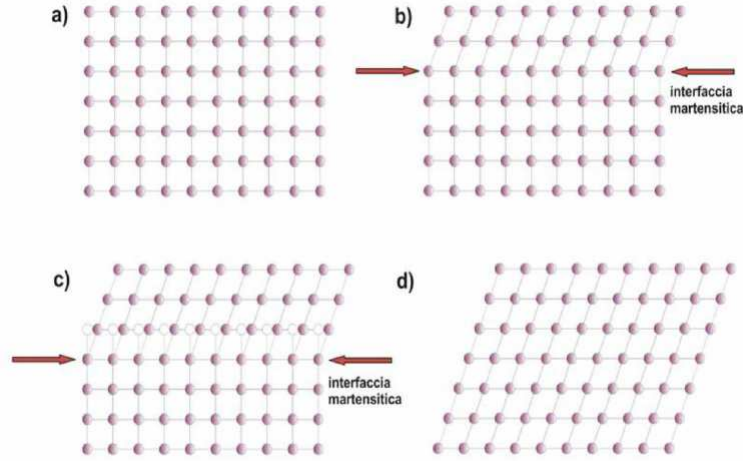


Figure 2.2: Two-dimensional schematization of the phase transformation from austenite to martensite, where a) is fully austenite and d) fully martensite. As shown in c), the atomic displacement occurs over short distances, such as not involve the breaking of chemical bonds.

phase. Under isothermal conditions, subjecting the material to a load (stress) growing, we can see a type of transformation called detwinning, in which the crystal structure is arranged according to the preferential directions of atomic lattices. Loading the specimen at a constant temperature, remains a permanent deformation. The high temperature causes a displacement of the atoms, the different forms of the martensitic state, settling in a regular and compact grid, as possible: the result is a cubic rigid provision to centred body (austenitic phase) and, from the macroscopic point of view, it attends to the recovery of the original shape of the SMA sample.

The martensite in region A has the same structure of martensite in region B, but exhibits different orientation. This assumption suggests that martensite can exist in two different configurations: stress-free martensite, characterized by a twinned multi-variant crystallographic structure, not related to any macroscopic deformation, and stress-induced martensite, characterized by a typical detwinned configuration with a single variant crystallographic structure, which aligns variants along a predominant direction, hence associated with macroscopic deformation. It is important to remark that the martensitic transformation in SMA consists mainly in a shear, without volume change [20][16]. The transition between different phases is the key to fully describe the behaviour of SMAs, and is clear that all the phenomenons are ruled by the strong connection between mechanical effects (loadings) and thermal effects (change in temperature).

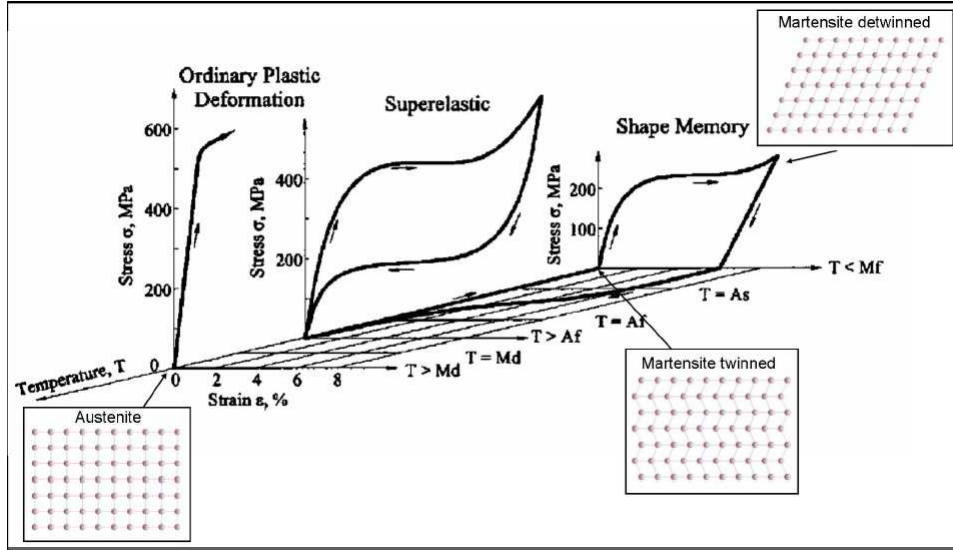


Figure 2.3: Thermomechanical cycle in a diagram load-strain-temperature representative of the memory one way effect.

2.2.2 Kink resistance

Kink resistance or, more appropriately, crush recoverability, is an important feature of NiTi-NOL, even more than PE and SME in some applications. When strains are locally increased beyond the plateau strain, stresses increase markedly. This causes strain to partition to the areas of lower strain, instead of increasing the peak strain itself. This phenomenon can be very dangerous for devices performances, and it is not uncommon in steel devices. In NiTi-NOL devices, kinking, or strain localization, is prevented by creating a more uniform strain than could be realized with a conventional material. This property is widely used in medical applications, especially in laparoscopic surgery, where the ability to lead the device through side branches or around sharp bends is vital.

2.2.3 Constant unloading stresses

The loading/unloading curves for SMA materials are essentially flat for a high range of deformations. This feature opens way for the realization of medical devices that are able to achieve a constant force in correspondence with a very wide range of deformations. In fact stresses observed in a NiTiNOL device are, for a wide range of strains, temperature-driven and not strain-driven as in conventional materials.

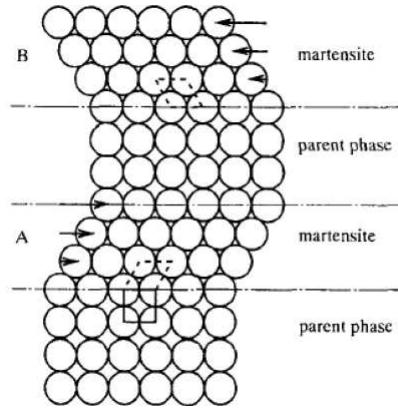


Figure 2.4: A schematic model of martensitic transformation.

2.2.4 Biocompatibility

This feature is obviously related to medical application and can be roughly defined as the ability of a material to be not rejected by the human body. Biocompatibility is directly related to the corrosion behaviour of the material in a specified solution and the tendency for the alloy to release potential toxic ions. Experimental studies, generally indicate that Nitinol has extremely good biocompatibility. This is due to the tendency of Nitinol surfaces to be covered with TiO_2 oxides with only a minor amount of nickel under normal conditions (Corrosion Resistance). The TiO_2 layer has a double purpose:

- Increase in the stability of the surface layers by protecting the bulk material from corrosion;
- Creation of a chemical barrier against Nickel oxidation, potentially toxic for the organism.

2.2.5 Hysteresis

One of the more unusual features that are found in Nitinol is the presence of a marked hysteresis in stress. In most materials, in fact, the stress grows linearly with the increase of the deformation during the process of loading, and decreases following the same path during the discharge process (Fig.2.5) Nitinol behaves differently: after an initial phase in which the stress increases linearly with the deformation, it has a phase in which the strain grows very little in front of a large deformation (plateau load). The end of this plateau is in correspondence of a deformation equal to about 8%. At this point, the stress starts growing linearly with the deformation. If at the end of plateau begins downloading, the stress decreases rapidly before

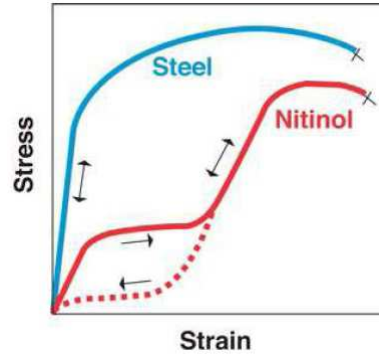


Figure 2.5: Comparison between the stress-strain diagram of Nitinol (in red) and that of steel (in blue).

settling on a unloading plateau, which has a value significantly lower than that of the load (also 25%). The presence of this hysteresis so accentuated, is exploited in the self-expanding stent. The force exerted by the stent on the vessel is low but if there are contractions of the vessel or compressions external, the stent manifests a resistance to deformation much higher.

2.2.6 Fatigue resistance

It is well known that Nitinol offers exceptional fatigue resistance in high strain, strain-controlled environments, while it may well fatigue rapidly in stress-controlled environments. Practically speaking, most fatigue environments in the body involve irregular cyclic motion against highly compliant tissue, and thus are a combination of stress and strain-control. Fatigue is also complicated by the superposition of a mean stress or strain on top of the cyclic component. As example of NiTiNOL fatigue study, the rotary bending fatigue properties of medical-grade Nitinol wires were investigated under conditions of 0.5–10% strain amplitudes to a maximum of 10^7 cycles. The results from this study provide insight into the behaviour of Nitinol under fully reversed fatigue conditions for three compositions, two surface conditions and three test temperatures. It was further observed that the strain amplitude to achieve 10^7 -cycles increases with both decreasing test temperature and increasing transformation temperature. Fatigue behaviour was not, however, strongly influenced by wire surface condition[3].

2.3 Nitinol

In 1962 is the discovery of the properties of nickel-titanium alloy, which has since known by the acronym of Nitinol, in honour of the laboratory where the scientist working at the

time of discovery (Naval Ordnance Laboratory in White Oak in Maryland). Over the past three decades, the binary alloys of Ni-Ti have been studied thoroughly and today are shape memory alloys most important from the commercial point of view, thanks to the excellent performance in terms of shape memory and superelasticity of the good mechanical properties. The shape memory alloy is a Ni-Ti binary intermetallic and equiatomic compound. The excellent biocompatibility combined with high resistance to corrosion, have made NiTi alloys practically the only materials perfectly tolerated by the human cells and able to work in harmony with the body. Indeed, even in patients allergic or sensitive to nickel, the risk of reaction is practically zero, thanks to the strong intermetallic bond that unites firmly the item to Ti. The corrosion resistance of Nitinol, as well as the Titan and other steels, is related to the ability of the material to become covered spontaneously one stable layer of titanium dioxide (TiO_2): This process takes the name of passivation. The Ni-Ti alloy also possesses characteristics that can be activated electrically by Joule effect: when an electric current passes through it, it generates sufficient heat to induce a phase transformation. For some years now the cost of production of the material went decreasing and increasing availability of commercial alloys, thereby the preconditions for the dissemination of the material in different technological areas.

2.3.1 Nitinol biomedical applications

Shape memory alloys, and in particular NiTi alloys, are characterized by two unique behaviours, thermally or mechanically activated: the shape memory effect and pseudo-elastic effect. These behaviours, due to the peculiar crystallographic structure of the alloys, assure the recovery of the original shape even after large deformations and the maintenance of a constant applied force in correspondence of significant displacements. These properties, joined with good corrosion and bending resistance, biological and magnetic resonance compatibility, explain the large diffusion, in the last 20 years, of SMA in the production of biomedical devices, in particular mini-invasive techniques. In this work a detailed review of the main applications of NiTi alloys in dental, orthopaedics, vascular, neurological, and surgical fields is presented. However, it is fundamental to remember that the complexity of the material and application requires a strict collaboration between clinicians, engineers, physicists and chemists for defining accurately the problem, finding the best solution in terms of device design and accordingly optimizing the NiTi alloy properties. NiTi-based alloys (with 48–52% in weight of Ni) associate shape-memory and pseudo-elastic effects, which are characterized by large plateau and stress hysteresis, with good workability in the martensite phase and good resistance to corrosion and fatigue; accordingly, nowadays most of SMA devices are produced with these alloys. Their use in biomedical applications is also suggested by their good biocompatibility

Fields of application	Effects	
	Pseudoelasticity	ShapeMemory Effect
	Mechanical shape recovery/wide plateau/constrained recovery	Heat-induced shape recovery/constrained recovery
Orthodontic field	Wires, palatal arches, distractors, endodontic files	Wires
Orthopedic field	Intraspinal implants, intramedullary nails	Staples or plates, devices for correcting scoliosis, spinal vertebrae spacer, intramedullary nails, devices for physiotherapy
Vascular field	Venous filters, devices for closing ventricular septal defects, self-expandable vascular stents, stent-graft, percutaneous devices to treat valvular diseases	Venous filters, devices for closing ventricular septal defects
Neurosurgical Field	Coils, stents, microguidewires	
Surgical field		Mini-invasive surgical instruments

Table 2.1: Sketch of the main NiTi applications in the biomedical field according to SMA properties.[27]

and excellent magnetic resonance and computer tomography compatibility. [1, 27, 24, 27, 22] Moreover, the mechanical behaviour of NiTi is more similar to biological tissue response[26] if compared with that of other metallic materials commonly used for biomedical devices, as stainless steel 316L and chromium-cobalt (Cr-Co) alloys. The device production procedure may strongly influence material characteristics; for this reason it is important to specify for which application the material is prepared. Medical NiTi alloy applications includes:

- Orthodontic applications. The first application of NiTi in the biomedical field dates back to 1975 when Dr. Andreasen from Iowa University made the first implantation of an orthodontic device exploiting the pseudo-elastic property of the alloy. [2] NiTi wires, which are in austenitic phase at the temperature of the buccal cavity, have been successfully used for years in fixed orthodontic treatment with multibrackets. In particular, pseudoelasticity is exploited for generating constant force, after positioning of the wire into the brackets, for wide dental movements. The shape memory effect, and

in particular the “constraint recovery” effect, is exploited for producing wires that are in martensitic phase during the positioning into the buccal cavity: deformed during the insertion into brackets, they try to recover the original undeformed shape whenever the patient ingests hot food or drinks. Because the recovery is prevented, the wires exert light forces on the teeth for the entire period in which the temperature is above the normal values. Pseudoelastic behaviour is also exploited for producing orthodontic distractors, which are used for solving the problem of teeth overcrowding in the mandible district: after a mandibular symphyseal distraction osteogenesis, the device is applied in order to produce an expansion of the mandible. Also in this case the use of SMA assures tensile forces nearer to the physiological values and constant in time. These forces create stress conditions that improve the tissue growth and hence teeth movement into the correct position.

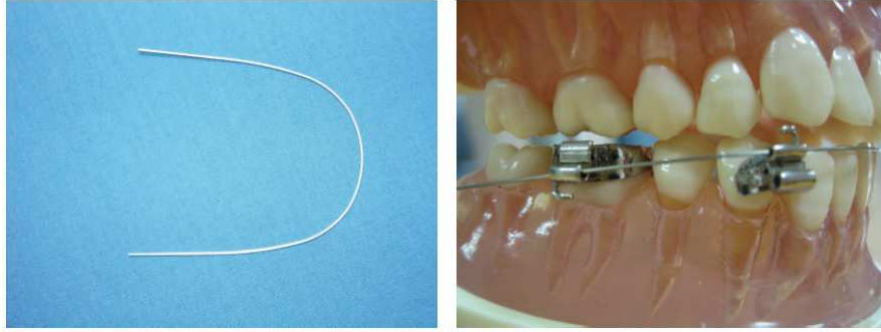


Figure 2.6: SMA orthodontic wires.

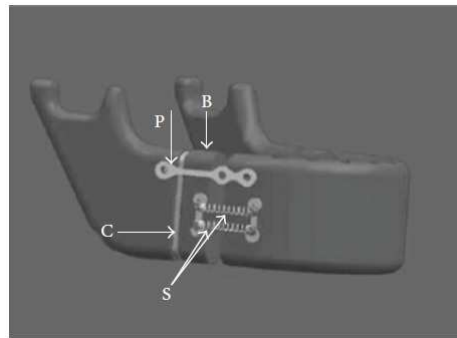


Figure 2.7: SMA orthodontic distractors. [27]

- Orthopaedic applications. The stress generated by SMA, when the shape recovery is constrained during heating from M_f to A_f , is exploited for fracture treatment by using orthopaedic staples or plates.[15] The device (Figure 2.8 (a)), characterized by a tempera-

ture A_f lower than that of the body, is deformed in the martensitic phase ($T \leq M_f < A_f$) and hence inserted into the body where the fracture is present. The body temperature induces the shape memory effect; because of the constrained recovery, the plates induce a constant stress, consequently joining the two fractured pieces. NiTi rods are also in-



Figure 2.8: Fig.(a) NiTi plate for mandible fracture, Fig.(b) spinal vertebrae spacer. [27]

serted in devices for correcting scoliosis; in this case, the constrained recovery is used for modifying vertebrae relative position; It has also been proposed [1] to exploit the shape memory effect (Figure 2.8 (b)) for designing a spinal vertebrae spacer with a rounded shape to be used on behalf of the damaged inter-vertebral disc. By exploiting the material's high deformability in martensitic phase, it is possible to modify the device shape for facilitating the insertion between the vertebrae where, being that the temperature is higher than A_f , the device recovers to its original shape. Another recent application of SMA in the orthopaedic field refers to SMA foams. Porous NiTi, characterized by low density, high surface area, high permeability, high strength (important to prevent deformation or fracture), relatively low stiffness (useful to minimize stress shielding effects), high toughness (essential to avoid brittle failure), and by a shape-recovery behaviour (facilitating implant insertion and ensuring good mechanical stability within the host tissue), is particularly interesting for osteointegration processes.

- Vascular applications. Besides the orthodontic field, the SMA devices are broadly applied in the vascular one. In particular, the introduction of the shape memory alloys boosted the development of mini-invasive techniques where the pathology is treated by the percutaneous insertion of the device rather than surgical intervention. The first vascular SMA application was the venous “Simon filter” (Figure 2.9) used to prevent emboli in patients unable to tolerate anticoagulants. It can be inserted thanks to the shape memory effect.[17] The device is produced in the open configuration with a NiTi alloy

having A_f equal to the body temperature, which depicts it in the martensitic phase at ambient temperature. Thus, during the crimping of the device on the catheter, a residual deformation is present as-consequence of the martensitic transformation from multi-variant to single-variant phase, which allows the device to be closed and easily placed in the catheter. A saline solution flows in the catheter to keep the temperature low during its insertion into the body. When the catheter is in position, the filter is released, the saline solution is stopped and the body heat induces the martensite-austenite transformation with recovery of the device's original shape. The filter is now able to block the possible clots of the blood stream. In literature, it is possible to find a variety of different filters [4] which use the pseudoelastic effect; similarly in this situation, the open configuration at ambient temperature is already in a stable austenitic phase; the crimped device, as soon as it is released in the body, recovers to its original open configuration. NiTi alloys are also used in numerous applications of the self-expandable vascular stents.

2.10 Stents are metallic "nets" (built by means of laser cutting stainless steel, Cr-Co, or NiTi alloy tubes) which open a stenotic vessel (obstructed by atherosclerotic deposits), therefore allowing restoration of the blood stream to peripheral tissues. For the NiTi stent, the stenting procedure consists of: (i) crimping the stent into the catheter in the austenitic phase (A_f is lower than body temperature) by means of a protective sheath, (ii) insertion of the catheter as stated above and (iii) removal of the sheath and expansion of the stent which tries to recover its original shape thereby enlarging the stenotic vessel. During this phase, the inverse transformation from martensite to austenite occurs, which is due to the martensitic instability at a temperature higher than A_f . The advantage of the self-expandable stent with respect to the stainless steel one is that it does not need balloon expansion which possess the risks of further damage of the vascular tissue due to its inflation, it does not require an over-expansion to account for the elastic recoil, and, when positioned, it exerts on the artery a constant force (due to the plateau) unless the artery does not try to occlude the device. Self-expandable stents are used to treat atherosclerotic lesions in the coronary arteries, the carotid arteries, and in the peripheral arteries, such as the iliac and femoral arteries. Another successful application of the NiTi alloys is the use of the stent-graft for the treatment of abdominal aortic aneurysms (AAA) [14]. For the treatment of this pathology, in conjunction with classical surgical techniques, Endovascular techniques, with the percutaneous insertion of stent-graft, gained popularity. This means that the stent-graft is easily crimpable on a catheter, sufficiently flexible during the insertion phase, and able to recover its original shape anchoring to the aorta once it has been positioned correctly. All of these features are present in the pseudoelastic behaviour of the NiTi alloys. A recent and very promis-

ing field of SMA application is related to the stenotic and regurgitant cardiac valves [8]. The use of mini-invasive techniques allows the surgeon to reduce, in a significant way, the risks of the procedure. For this reason, there are different companies which are developing percutaneous devices to treat mitral, pulmonary, and aortic valvular diseases.

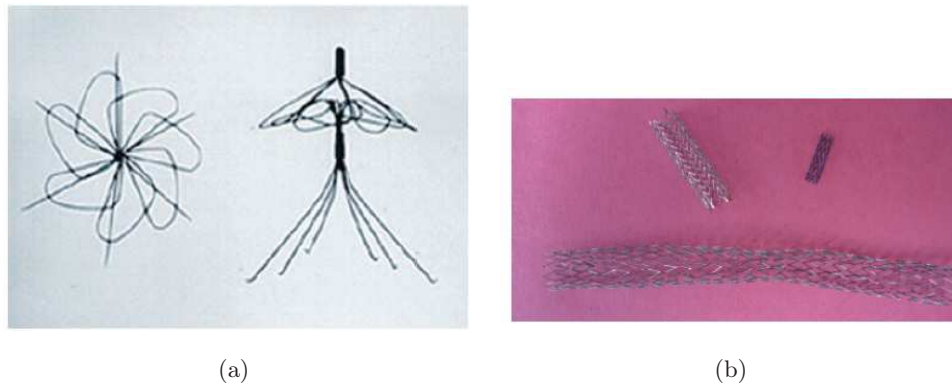


Figure 2.9: Fig.(a) Venous filter: Simon filter, Fig.(b) Example of SMA stents: (top right) coronary stent, (top left) carotid stent, (bottom left) femoral stent [27].



Figure 2.10: Example of stent-graft in NiTi alloys.[7]

- Neurosurgical applications. Nowadays, NiTi alloys in the neurosurgical field [9] are used for producing three types of devices: (1) coils, (2) stents and (3) microguidewires. Coils are devices used for the treatment of cerebral aneurysms, which are localized dilations of the intra-cranial arteries. Coils are wires that are positioned into the aneurysm as a

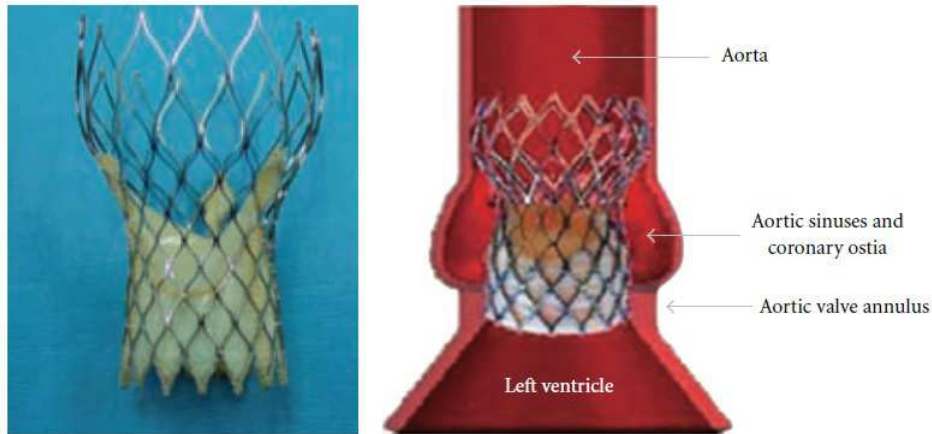


Figure 2.11: CoreValve aortic valve <http://www.medtronic.com/corevalve/ous/index.html>.

ball to induce clotting or thrombotic reaction within the aneurysm that, if successful, will eliminate the risk of rupture. Stents are also used for the treatment of intra-cranial atherosclerotic disease. The stent treatment aims to recover the original blood flow where there is a narrowed lumen. Moreover, microguidewires used for stent positioning may be made of NiTi with the advantage of obtaining a higher strain recovery and torsion resistance as well as a better stress distribution (due to the plateau in the stress-strain curve), which reduces the guidewire bending problems.

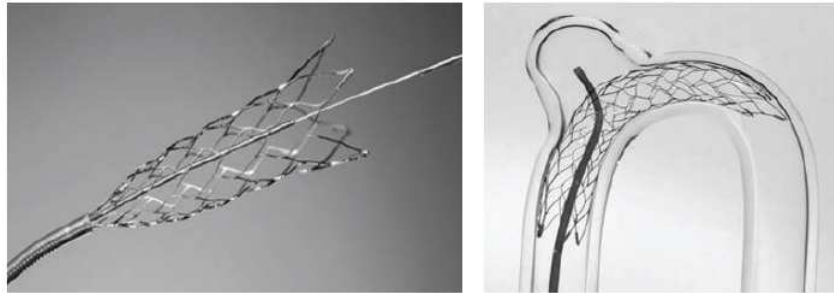


Figure 2.12: NiTi self-expandable neurosurgical stent (Enterprise Vascular Reconstruction Device; Cordis Corp., Miami Lakes, FL) [27].

2.4 Nitinol literature

The aim of the present work is to investigate Nitinol behaviour by considering the influence of the various used parameters from different authors. We used ABAQUS/Standard (v.6.12-1) finite element analysis package, in combination with Abaqus user-defined material subrou-

tine (UMAT), to perform material material behaviour and to determine local stresses and strains in a cube with nitinol material. At first we created a 1x1x1 mm cube subjected to tension-compression uni-axial test in x direction (figure 2.13), using different parameters which characterize Nitinol behaviour, from several literature papers.

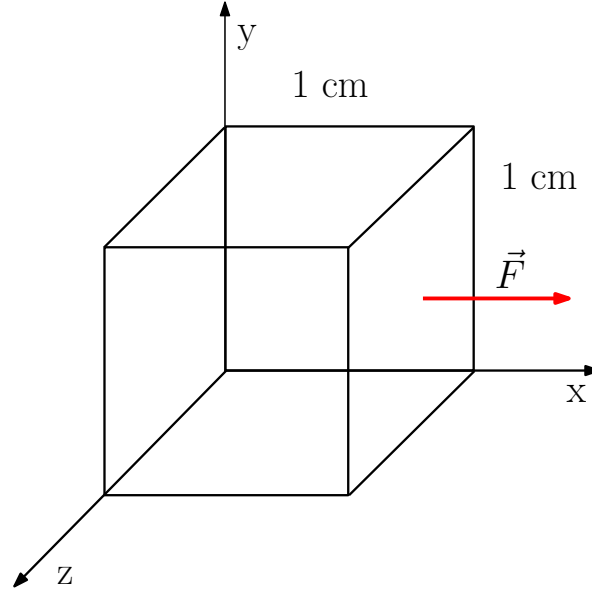


Figure 2.13: cube subjected to tension-compression uniaxial test in x direction

2.5 Pelton et al. 2013

In this article Pelton et al. [3] analyse the rotary bending fatigue properties of medical-grade Nitinol wires under conditions of 0.5–10% strain amplitudes to a maximum of 10^7 cycles. Self-expanding Nitinol stents are initially strained 6–10% during crimping, and inserted into a catheter delivery system, with a partial strain release with deployment into the diseased vessel. The stent is then subjected to multi-axial cyclic deformations with combinations of mean strain (from stent/vessel oversizing) and strain amplitude (from cardiac cycles and musculoskeletal motions). In contrast, the outer fibers of the endodontic wires are subjected to alternating compressive and tensile strains with a (nominal) net zero-mean strain for many thousands or even millions of cycles. We used this paper as reference to see the characteristic Nitinol stress-strain curve. The purpose of their research, therefore, is to report an investigation of the rotating bending fatigue characteristics of shape memory and pseudoelastic medical-grade Nitinol wires as part of a larger investigation of Nitinol fatigue behaviour. Starting from those information we use nitinol characteristic parameters from this paper to analyse nitinol behaviour.

Figure 2.14 shows the uni-axial stress-strain properties in tension and compression at $T=22^{\circ}\text{C}$, $T=37^{\circ}\text{C}$ and $T=60^{\circ}\text{C}$. We used only 15 constants to run UMAT subroutine in ABAQUS Standard. The curves show the expected differences in elastic modulus and plateau stress with increasing test temperature. Figure 2.15 provides the stress-strain and stress-temperature curves, while 2.2 lists the Nitinol material parameters.

Abaqus superelasticity UMAT constants	Extracted values
Austenite elasticity (MPa)	51437
Austenite poisson ratio	0.33
Martensite elasticity (MPa)	21588
Martensite poisson ratio	0.33
Transformation strain	0.037
$d\sigma/dT$ loading (MPa/ $^{\circ}\text{C}$)	5.1
Start transformation loading (MPa)	494
End transformation loading (MPa)	557
Reference Temperature ($^{\circ}\text{C}$)	22
$d\sigma/dT$ unloading (MPa/ $^{\circ}\text{C}$)	5.1
Start transformation unloading (MPa)	336
End transformation unloading (MPa)	311
Start transform stress compression (MPa)	755
Volumetric Transformation strain	0
Number of annealing steps	0

Table 2.2: ABAQUS UMAT Parameters.

2.6 Other references

Nitinol behaviour was analysed also for two other literature articles, only for traction. De Bock et al. [25] in their study details the virtual deployment of a bifurcated stent graft in a abdominal aortic aneurysm model, using finite element method with silicone as SMA material. Kleinstreuer et al. [6] present a finite element analysis of tubular, diamond-shaped stent graft under representative cyclic loading conditions for abdominal aortic aneurysm repair. They studied the effects of crimping, deployment and cyclic pressure loading on stent-graft fatigue life, radial force and wall compliance for realistic but different nitinol materials and grafts. The curves were plotted at $T=22^{\circ}\text{C}$, to compare the differences between parameters used by authors. As show in Fig.2.3, the various parameters implemented determine the difference

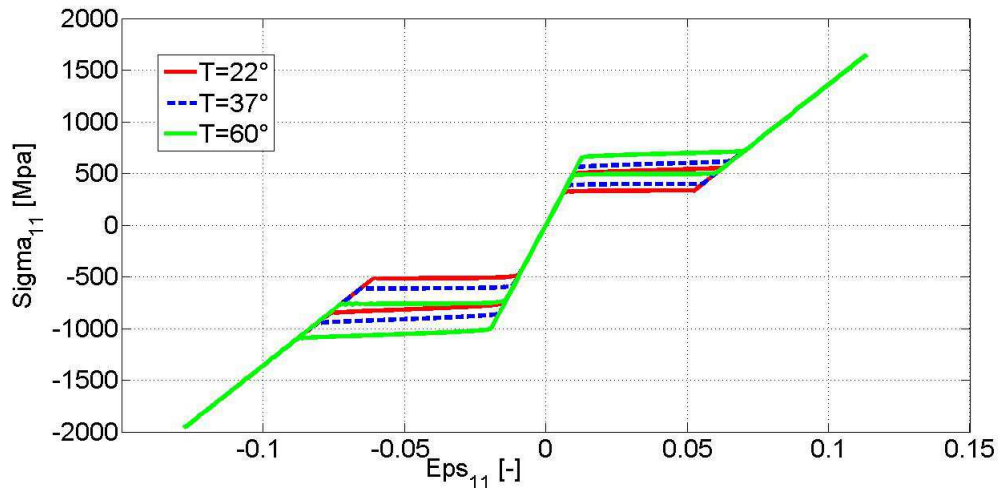


Figure 2.14: Pelton Review. Compare Nitinol behaviour for $T=22^\circ$, $T=37^\circ$ and $T=60^\circ$

representation of the curve. In De Bock et al. article the $d\sigma/dT$ loading and unloading terms were missed [6],[25].

Abaqus superelasticity UMAT constants	De Bock 2012	Kleinstreuer 2008	Pelton 2013
Austenite elasticity (MPa)	35850	51700	51437
Austenite poisson ratio	0.3	0.3	0.33
Martensite elasticity (MPa)	13950	47800	21588
Martensite poisson ratio	0.3	0.3	0.33
Transformation strain	0.0532	0.063	0.037
$d\sigma/dT$ loading (MPa/ $^\circ\text{C}$)	-	6.527	5.1
Start transformation loading (MPa)	480	600	494
End transformation loading (MPa)	640	670	557
Reference Temperature ($^\circ\text{C}$)	22	37	22
$d\sigma/dT$ unloading (MPa/ $^\circ\text{C}$)	-	6.527	5.1
Start transformation unloading (MPa)	270	288	336
End transformation unloading (MPa)	200	254	311
Start transform stress compression (MPa)	480	900	755
Volumetric Transformation strain	0	0.063	0
Number of annealing steps	0	0	0

Table 2.3: ABAQUS UMAT Parameters by different authors.

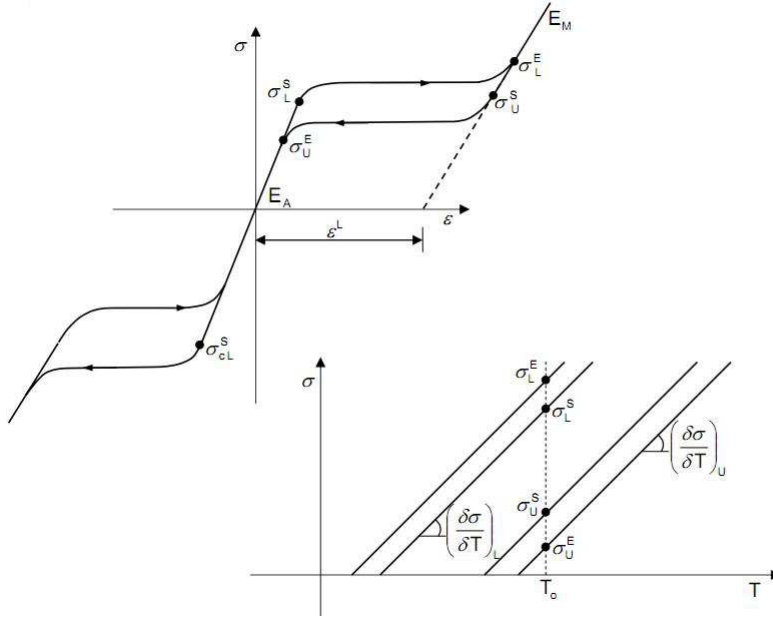


Figure 2.15: Nitinol material properties (from ABAQUS Nitinol UMAT). Nitinol parameters based on the uni-axial behaviour (from ABAQUS Nitinol UMAT)) where E_A Austenite elasticity, ν_A Austenite Poisson's ratio, E_M Martensite elasticity, ν_M Martensite Poisson's ratio, ϵ^L Transformation strain, $(\delta\sigma/\delta T)_L$ loading, σ_L^S Start of transformation loading, σ_L^E End of transformation loading, T_0 Reference Temperature, $(\delta\sigma/\delta T)_U$ unloading, σ_U^S Start of transformation unloading, σ_U^E End of transformation unloading, σ_{CL}^S Start of transformation stress during loading compression as a positive value, ϵ_V^L Volumetric transformation strain, N_A Number of annealing to be performed during the analysis. [6]

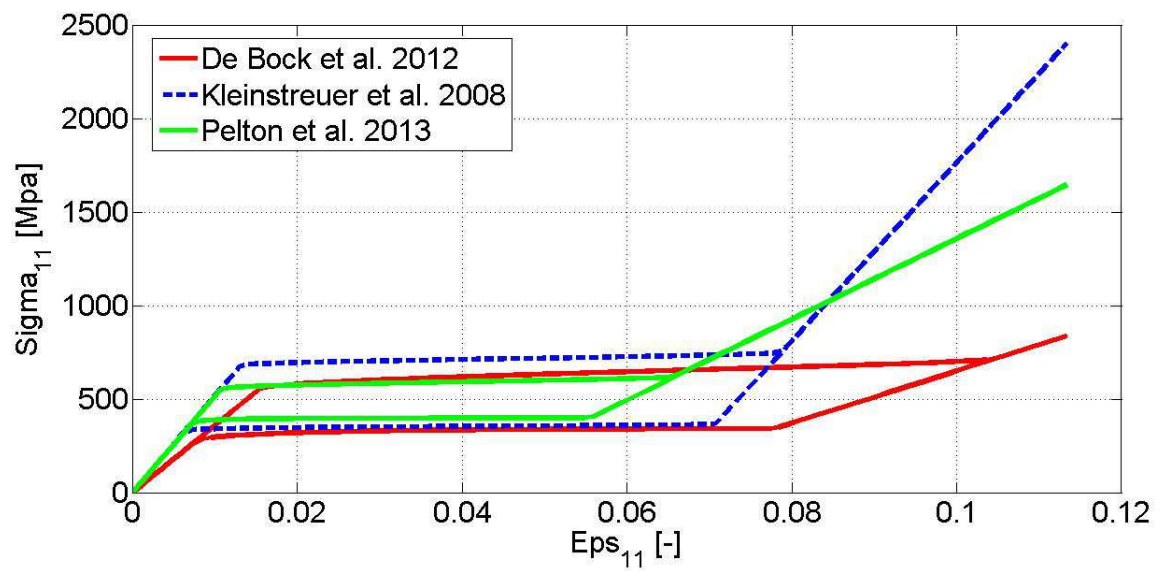


Figure 2.16: Compare Nitinol behaviour for $T=37^\circ$ by different authors.

Chapter 3

Endograft Model Kinematics

3.1 Introduction

Despite traditional open-surgery remains the gold standard to treat aortic pathologies, the use of minimally invasive endovascular techniques is rapidly arising in the recent years as a valuable alternative. In particular, endovascular aortic repair (EVAR) is getting predominant to treat patient with acute type B dissections and aortic aneurysms. One of the problems after the application of a self-expanding endograft in site, is to analyse where the stresses are concentrated, to see which are the most stressed device regions due to the cardiac cycle. So the next step is to develop a finite element analysis (FEA), relying on a multidisciplinary approach aimed at designing and optimizing patient-specific tailored prosthesis and procedure. Moving from such considerations, in the present study we calculate stress-strain values in characteristic stent regions with a finite element model and we compare results with those from post-operative computed tomography (CT) images. Starting from its shape at rest, the stent is crimped to be inserted within the catheter and once on site is partially released as a function of the diameter of the artery in which it is positioned. In this phase (deployment) the values of von Mises stress and strain associated with the stent are calculated. The numerical analysis is clearly non-linear, involving large deformation and contact; the settings of contact parameters is an important step for simulation convergence. The software used for finite element analysis is Abaqus/Standard and the steps followed for analysis are explained in details below. The reduction and enlargement of the diameter of the ring are obtained with a contact analysis with a rigid surface (catheter).

3.2 Finite element method (FEM)

3.2.1 Overview of the method

The finite element method (FEM) is a generalized procedure of continuum problems posed by mathematically defined statements. It consists on a group of numerical techniques able to compute approximate solutions of partial differential equations as well as integral equations. In FEM for structural analysis, the system geometry is divided into a number (often large) of discrete elements. These discrete elements are joined by entities called nodes. The set of nodes and finite elements is called the mesh. The number of elements for unit of length or area is called mesh density. In a stress analysis, the nodes displacements are the fundamental variables that a Finite Element solver, like Abaqus, calculates. Once the nodal displacements are known, the stresses and strains in each finite element can be determined easily. Nodal displacements can be obtained following two approaches:

- Implicit method. In this approach, the equilibrium equations need to be solved simultaneously to obtain the displacements of all the nodes. This requirement is best achieved by matrix techniques; therefore, the internal and external force contributions can be written as matrices. This system of equations can then be solved to obtain values of the unknowns nodal displacements. At this point is trivial to find the strain values and, passing through the constitutive relations, to calculate the stresses in all the elements. It is important to note that implicit FEM requires to solve the equations system at the end of each solution increment. Moreover, the resolution with an implicit method requires the creation of the global stiffness matrix and its inversion;
- explicit method. In contrast to implicit methods, an explicit method does not require the simultaneous solving of an equations system or the calculation of a global stiffness matrix. Instead, the solution is advanced kinematically from one increment to the next.

The choice between the two approaches can be guided by several reasons. For example, implicit methods result more efficient to solving smooth non linear problems; on the other hand, explicit methods are the clear choice for a wave propagation analysis. In the middle, there is a wide variety of problems well suited for both the approaches, typically static or quasi-static problems with complex contact issues. For these problems, implicit way shows an absolute stable scheme, but can results in an high number of iterations and computational cost. Concerning to explicit method, they do not require to determine the solution for the whole model at each increment, so the analysis can be more efficient. On the other hand, explicit approach needs particular care for the dynamic control, such as kinetic-internal energy ratio (for quasi-static analyses), that can reduce the time increment and the procedure can be less efficient.

Concerning on the computational cost the explicit method, shows a proportional relationship between computational cost and the number of elements and a roughly inversely proportional relationship with the smallest element dimension. Mesh refinement, therefore, increases the computational cost by increasing the number of elements and reducing the smallest element dimension. For the implicit method, computational cost prediction is more difficult in reason of the problem-dependent relationship between element connectivity and solution cost. Using the implicit method, experience shows that for many problems the computational cost is roughly proportional to the square of the number of degrees of freedom. The explicit method shows great cost savings over the implicit method as the model size increases, as long as the mesh is relatively uniform. Fig.3.1 shows a qualitative comparison of cost versus model size (in terms of degrees of freedom) using the explicit and implicit methods. For many models the number of elements is so high that an explicit approach is the only way to get the simulation results in a relatively short time.

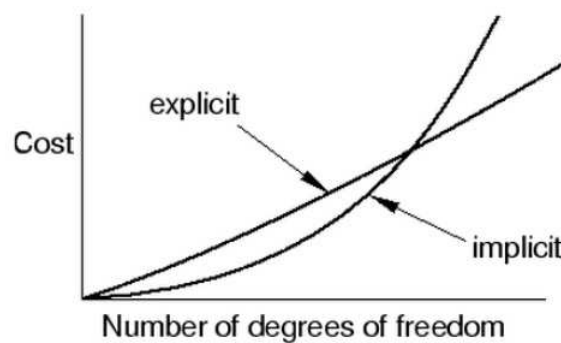


Figure 3.1: Qualitative comparison between implicit and explicit methods in terms of computational cost.

3.2.2 Abaqus software

Abaqus (Simulia, Dassault Systems, Providence, RI, USA) is a suite of powerful engineering simulation programs, based on the finite element method, that can solve problems ranging from relatively simple linear analyses to the most challenging nonlinear simulations. Abaqus contains an extensive library of elements that can model virtually any geometry. It has an equally extensive list of material models that can simulate the behaviour of most typical engineering materials including metals, rubber, polymers, composites, reinforced concrete, crushable and resilient foams, and geotechnical materials such as soils and rock. Designed as a general-purpose simulation tool, Abaqus can be used to study more than just structural (stress/displacement) problems. It can simulate problems in such several areas as heat trans-

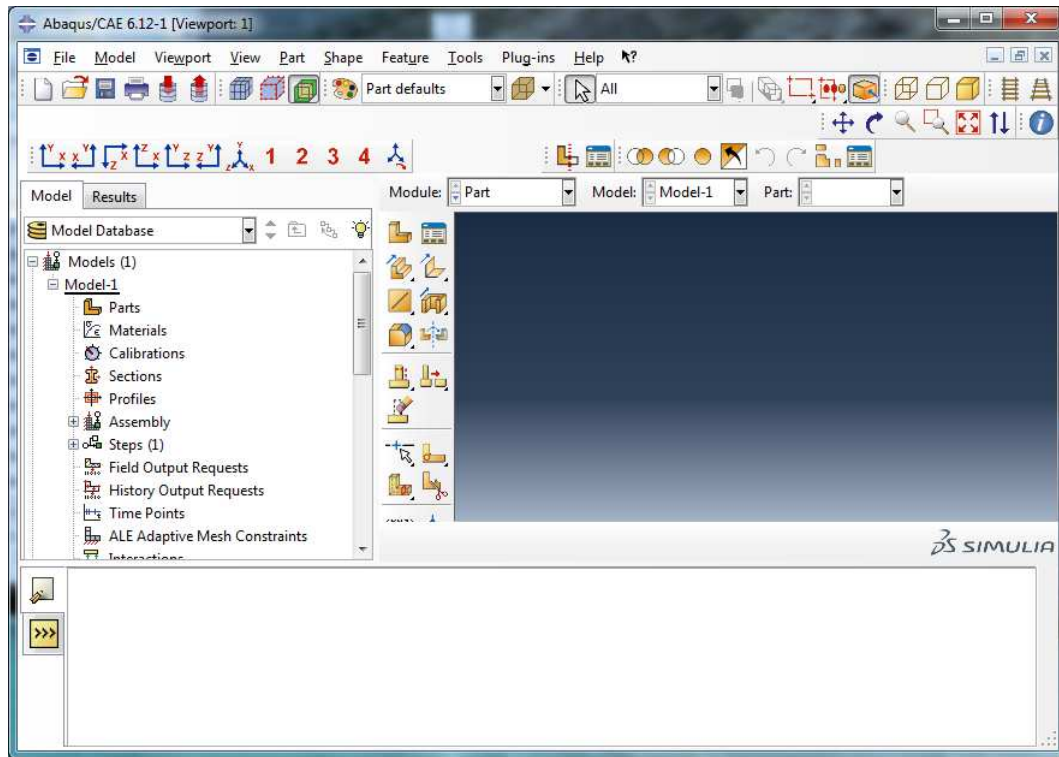


Figure 3.2: Abaqus interface

fer, mass diffusion, thermal management of electrical components (coupled thermal-electrical analyses), acoustics, soil mechanics (coupled pore fluid-stress analyses), piezoelectric analysis, electromagnetic analysis, and fluid dynamics.

Abaqus offers a wide range of capabilities for simulation of linear and nonlinear applications. Problems with multiple components are modeled by associating the geometry defining each component with the appropriate material models and specifying component interactions. In a nonlinear analysis Abaqus automatically chooses appropriate load increments and convergence tolerances and continually adjusts them during the analysis to ensure that an accurate solution is obtained efficiently. The Abaqus finite element system includes:

- Abaqus/Standard is a general-purpose analysis product that can solve a wide range of linear and nonlinear problems involving the static, dynamic, thermal, electrical, and electromagnetic response of components. Abaqus/Standard solves a system of equations implicitly at each solution “increment.” In contrast, Abaqus/Explicit marches a solution forward through time in small time increments without solving a coupled system of equations at each increment (or even forming a global stiffness matrix);
- Abaqus/Explicit is a special-purpose analysis product that uses an explicit dynamic

finite element formulation. It is suitable for modeling brief, transient dynamic events, such as impact and blast problems, and is also very efficient for highly nonlinear problems involving changing contact conditions, such as forming simulations;

- Abaqus/CAE, an interactive environment used to create finite element models, submit Abaqus analyses, monitor and diagnose jobs, and evaluate results;
- Abaqus/Viewer, a subset of Abaqus/CAE that contains only the postprocessing capabilities of the Visualization module.

A complete Abaqus analysis usually consists of three distinct stages:

- Preprocessing;
- Simulation;
- Postprocessing;

As shown in figure 3.3, Abaqus/CAE is a complete Abaqus environment that provides a simple, consistent interface for creating, submitting, monitoring, and evaluating results from Abaqus/Standard and Abaqus/Explicit simulations. Abaqus/CAE is divided into modules, where each module defines a logical aspect of the modeling process; for example, defining the geometry, defining material properties, and generating a mesh. As you move from module to module, you build the model from which Abaqus/CAE generates an input file that you submit to the Abaqus/Standard or Abaqus/Explicit analysis product. The analysis product performs the analysis, sends information to Abaqus/CAE to allow you to monitor the progress of the job, and generates an output database. Finally, you use the Visualization module of Abaqus/CAE (also licensed separately as Abaqus/Viewer) to read the output database and view the results of your analysis.

3.2.3 Server information: cineca

The used server to perform the analysis of Abaqus is called cineca. Founded in 1969 (as the Interuniversity Consortium for Automatic Computation North-Eastern Italy), today CINECA - Interuniversity Consortium is the largest computing center in Italy, one of the most important in the world. Operating under the control of the Ministry of Education, University and Research, provides support to the activities of the scientific community through supercomputing and its applications, develops systems management for university administrations and the Ministry of Education, designs and develops information systems for public administration, health and business. One very important goal of Cineca is supporting scientific and

technological research with computational tools. To this goal we make available the most modern and effective System Software and programming environments in addition to a large and etherogeneous library of Scientific Application Software for different disciplines. Eurora

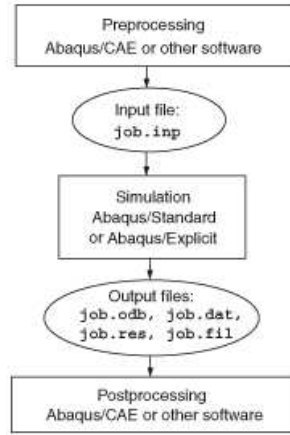


Figure 3.3: Abaqus analysis flow.

3.3 Simulation strategy

Despite the fact that endografting is a complex procedure characterized by several steps, this study focuses mainly on the *crimping* and *deployment* endoprosthesis : consequently, we include only the following parts in our simulation:

- catheter model, figure 3.4;
- endoprosthesis model, figure 3.5;

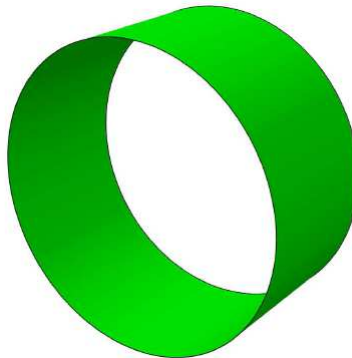


Figure 3.4: Cylindric surface representation used for the catheter model.

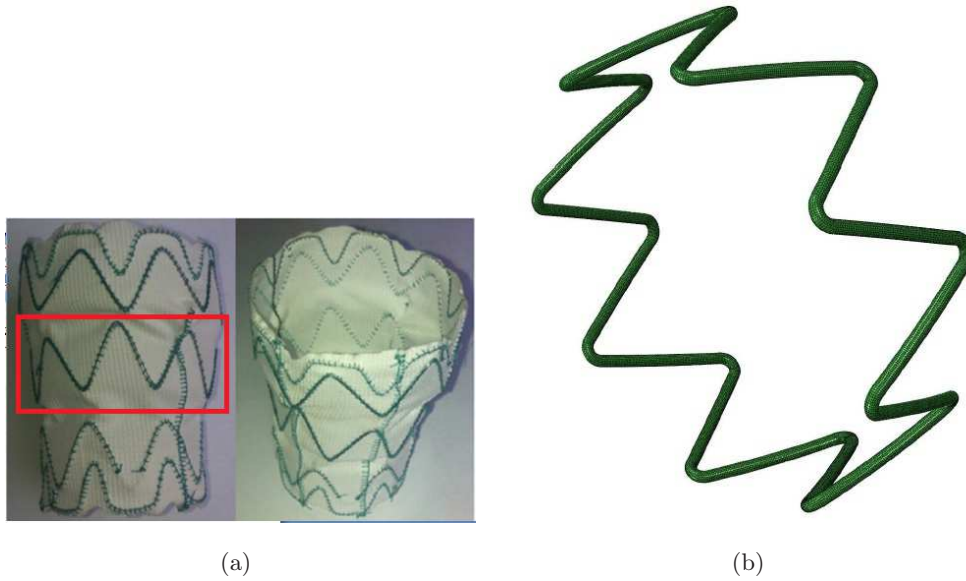


Figure 3.5: Fig.(a): Real device. Fig.(b): Final finite element model (only central ring).

3.3.1 Preprocessing: creating the model with Abaqus/CAE

In this section we discuss how to use Abaqus/CAE to create the entire model for this simulation. Abaqus/CAE is divided in different modules and each of those is used to build the model. The first step in creating the model is to define its geometry.

Part

In the create dialog box we create two parts:

- central ring of the 3D stent;
- cylindrical rigid surface (catheter).

The stent has been realized taking advantage of the modularity of its components. Starting from a simple parts of it, it was possible to reproduce its parts as to realize the entire central ring. The diameter of the ring was 38mm, the same diameter as real device. We modelled the stent as a 3D deformable, extruded solid. To pass from planar stent configuration to three-dimensional stent configuration it was necessary to use a script in Matlab that should convert the coordinates of the nodes in the planar configuration in three-dimensional ones. To model the catheter we used a cylinder with 40mm of diameter, more than stent diameter because at the beginning the two parts must not come into contact. The catheter is modelled as a rigid body defined by a surface obtained by sweeping a cylindrical section. In figure 5.4 we can see the planar stent and 3D stent representation.

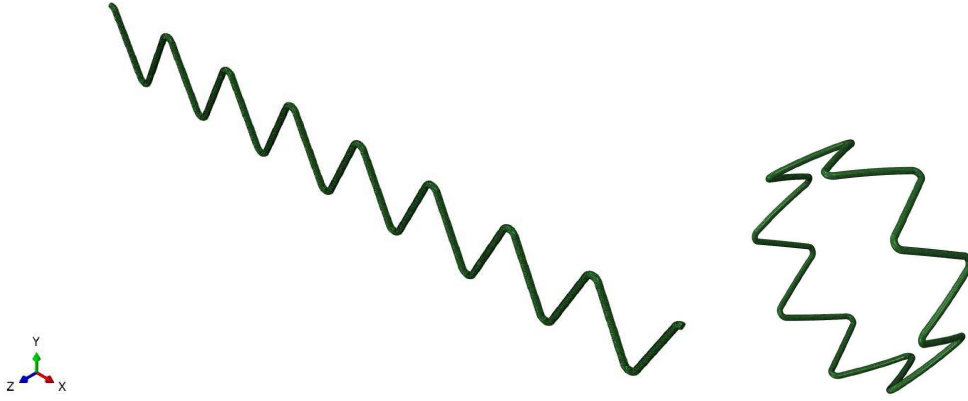


Figure 3.6: Planar stent (left) and 3D stent (right) representation.

Material and section properties

The next step in creating the model involves defining and assigning material and section properties to the part. Each region of a deformable body must refer to a section property, which includes the material definition. To reproduce the super-elastic material response for stent model, we use the Abaqus user material subroutine of the super-elastic model originally proposed by Auricchio and Taylor [11] [12]. The adopted Nitinol constitutive parameters are those reported in the Table 3.1. The section assigned for stent is solid homogeneous.

Assembly and step modules

An assembly contains all the geometry included in the finite element model. Each Abaqus/CAE model contains a single assembly. The assembly is initially empty, even though we have already created a part. We will create an instance of the part in the Assembly module to include it in our model. In our analysis we include both stent and cylindrical rigid surface, because our goal is analyse them together. Since interactions, loads, and boundary conditions can be step dependent, analysis steps must be defined before these can be specified. For this simulation we will define a single static, general step. In addition, we will specify output requests for your analysis. These requests will include output to the output database (.odb) file. In this case we create two step:

- crimping step: in this step we simulated the diameter reduction of the stent, representing the moment when the stent is inserted within the catheter. The time period is 1 second, the initial increment size is 0.001 s and minimum is $1 * 10^{-11}$ s.
- deployment step: in this step we simulated the diameter enlargement, which represents the time when the stent is released from the region involved in aortic disease, to isolate

Abaqus superelasticity UMAT constants	Extracted values
Austenite elasticity (MPa)	51 700
Austenite poisson ratio	0.3
Martensite elasticity (MPa)	47 800
Martensite poisson ratio	0.3
Transformation strain	0.063
$d\sigma/dT$ loading (MPa/°C)	6.527
Start transformation loading (MPa)	600
End transformation loading (MPa)	670
Reference Temperature (°C)	37
$d\sigma/dT$ unloading (MPa/°C)	6.527
Start transformation unloading (MPa)	288
End transformation unloading (MPa)	254
Start transform stress compression (MPa)	900
Volumetric Transformation strain	0
Number of annealing steps	0

Table 3.1: ABAQUS UMAT Parameters.

it. The used parameters are the same as the previous step. Since we will use the visualization module to post-process the results, we must specify the output data we wish to have written to the output database file. Default history and field output requests are selected automatically by Abaqus/CAE for each procedure type. In this case we selected only stress, strain and displacement variables.

Interaction

We used the interaction module to define and manage constraints between regions of a model. In this case we used contact to impose stent deformation from crimping to deployment. The contact between two surfaces is very hard for convergence analysis, and parameters must set precisely to have convergence. The interaction type is surface-to-surface. Surface-to-surface contact interactions describe contact between two deformable surfaces or between a deformable surface and a rigid surface. A contact interaction property can define tangential behaviour (friction and elastic slip) and normal behavior (hard, soft, or damped contact and separation). In addition, a contact property can contain information about damping, thermal conductance, thermal radiation, and heat generation due to friction. A contact interaction property can be referred to by a general contact, surface-to-surface contact, or self-contact interaction. The

contact properties are:

- tangential behaviour: the friction formulation is penalty, the fraction of characteristic surface dimension is 0.005 and the friction coefficient was imposed to 0.
- normal behaviour: the pressure-overclosure is set to hard contact (classical Lagrange multiplier method of constraint enforcement in an Abaqus/Standard analysis), the penalty is the constraint enforced method and the stiffness scale factor is 0.01.
- geometric properties: the out-of-plane surface thickness or cross-sectional area is set to 1.

The penalty method approximates hard pressure-overclosure behaviour. With this method the contact force is proportional to the penetration distance, so some degree of penetration will occur. Advantages of the penalty method include:

- Numerical softening associated with the penalty method can mitigate overconstraint issues and reduce the number of iterations required in an analysis.
- The penalty method can be implemented such that no Lagrange multipliers are used, which allows for improved solver efficiency.

Boundary conditions

For our analysis boundary conditions set are:

- Displacement/rotation with cylindrical coordinates imposed of two superior stent node to prevent the stent from moving in the rho direction;
- Displacement/rotation with cylindrical coordinates imposed of eight superior stent nodes to prevent the stent from moving in the zeta direction;
- Displacement/rotation with cylindrical coordinates imposed to cylindrical rigid surface to allow displacement during the analysis. In the first step the catheter was crimped with a imposed displacement set as -13 mm on the radial direction, to crimp the stent and in the deployment stent configuration was imposed a displacement set as -5 mm, to enlarge the stent diameter.

Mesh definition

The Mesh module allows we to generate meshes on parts and assemblies created within Abaqus/CAE. Various levels of automation and control are available so that we can create a

mesh that meets the needs of your analysis. As with creating parts and assemblies, the process of assigning mesh attributes to the model—such as seeds, mesh techniques, and element types—is feature based. As a result we can modify the parameters that define a part or an assembly, and the mesh attributes that you specified within the Mesh module are regenerated automatically. The catheter surface was meshed with 3750 three-dimensional, 4-node surface elements with reduced integration (SFM3D4R) and the stent model was meshed with 120075 nodes and 102400 8-node linear brick element (C3D8).

3.3.2 Results

The numerical analysis is non-linear, involving large deformations and contact; we use Abaqus/Standard (Simulia, Dassault Systemes, Providence, RI, USA) as finite element solver. In our simulation strategy, as already proposed in different studies [12] [10], the endograft deformation is driven by the configuration change of the catheter, imposed by displacement boundary conditions on its nodes, determined as the difference between a starting and final catheter configuration for each simulation step. In particular, the simulation consists of two main stages:

- Endograft crimping. Starting from a straight configuration the catheter is gradually crimped following the endograft centerline and leading to the endograft deformation;
- Endograft deployment. From the crimped configuration, the catheter is re-enlarged and the endograft expands.

As we can see in figure 3.8 and 3.7, the von mises values are comparable to literature [10, 12]. We obtained comparable values from literature also for strain, visualised in figure 3.11. We can analyse the stress mean distribution during crimping analysis and deployment step respect with number of meshed elements, figure 3.9. With respect Auricchio et al. paper[10] von mises stress calculated in this section are comparable. Kleinstreuer et al. [6] found stress values lower than ours, but is not specified in which step analysis they are performed. As we can see in the figure 3.9, the stress values associated with the deployment steps are lower compared to the values of the stress in crimping step, as we expected. The number of items associated with higher values of stress in crimping and deployment are comparable. The considerations can be made for logarithmic strain values, shown in figure 3.12. In this case the number of elements are higher for strain values in deployment step, for logarithmic strain values between 0 and 0.005.

The presented approach is the standard used method in the literature to evaluate the stress and strain values in aortic stent-graft before and immediately after implantation of the device.

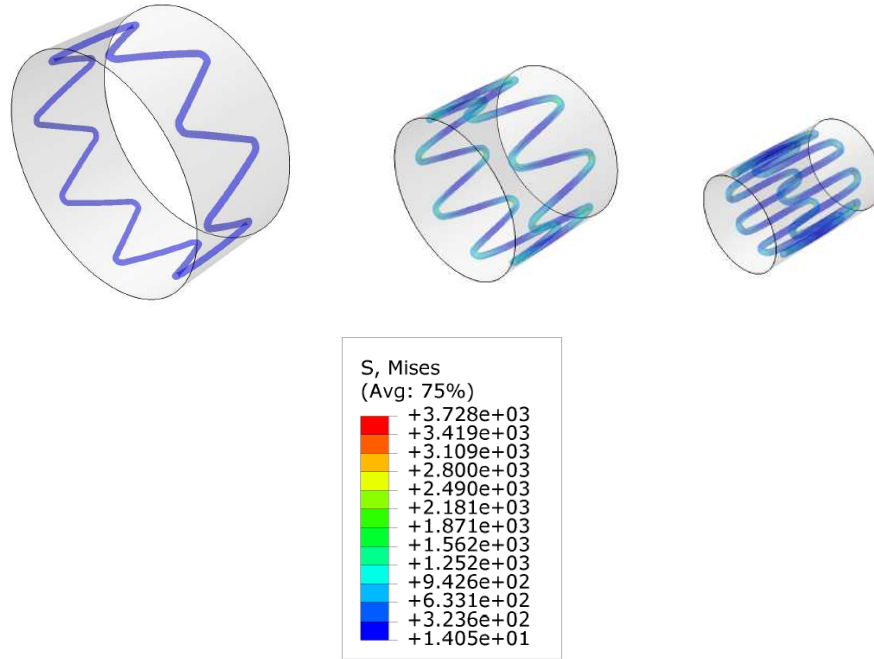


Figure 3.7: Crimping analysis steps (left to right). Stress values are calculated for maximum crimping state.

In this case it is an approach entirely ideal. The next step is going to analyse the postoperative CT images and from these extract the needed information to go from an idealized analysis to an more realistic 'patient-specific' analysis . By positioning our model as the implanted stent, through a roto-translation, we reached the starting condition in order to analyse CT images. Once obtained the same experimental conditions of the implanted device, we can analyse the stresses to which it is subjected and in which regions these stresses are most concentrated.

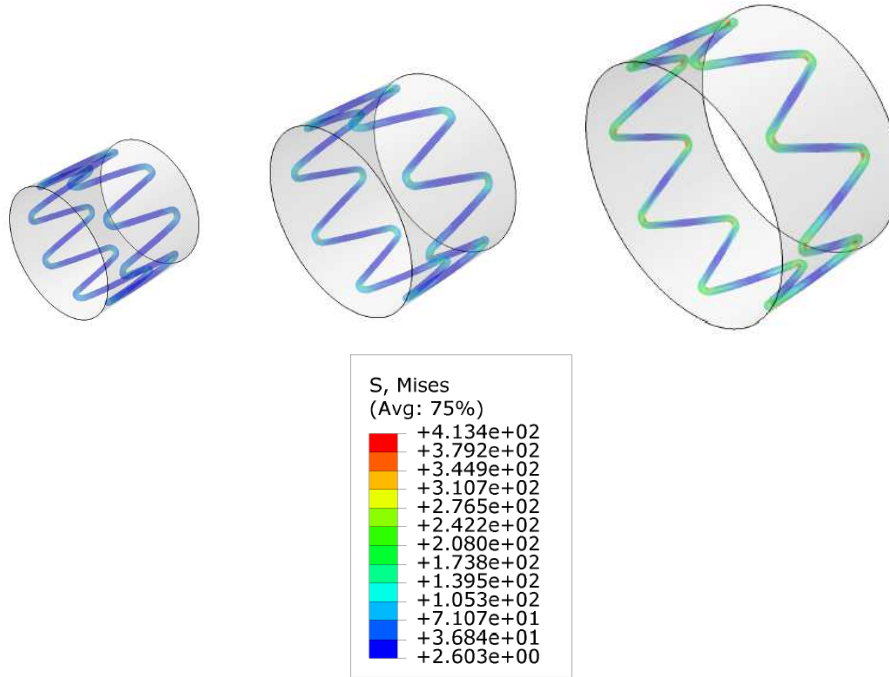


Figure 3.8: Deployment analysis steps(left to right). Stress values are calculated for maximum deployment state.

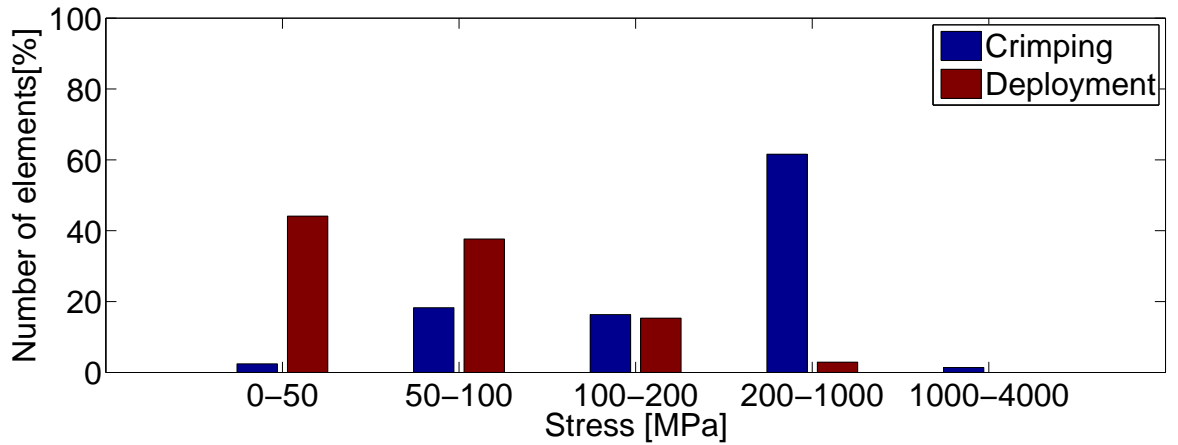


Figure 3.9: Histogram of von mises stress distribution during crimping step and deployment step, compared to number of elements which have those stress values in 8 characteristic integration points for each element. The stress values are plotted as the mean for each integration point and are calculated in MPa units. The number of elements are normalised respect with maximum number of elements.

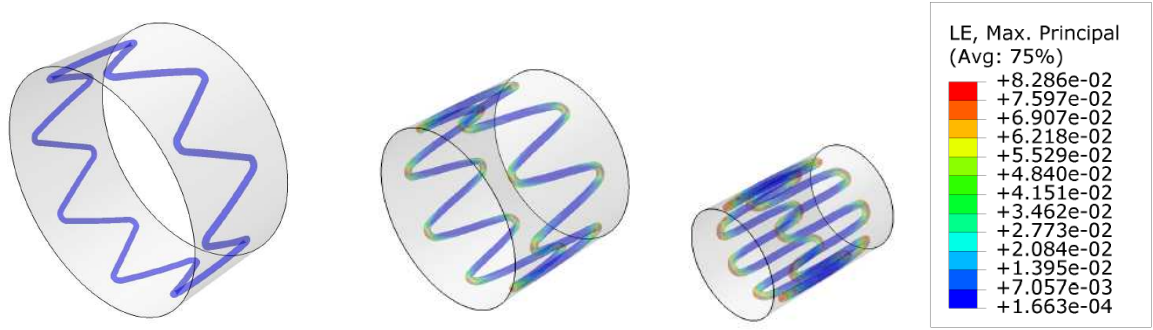


Figure 3.10: Crimping analysis steps (left to right) with logarithmic strain values.

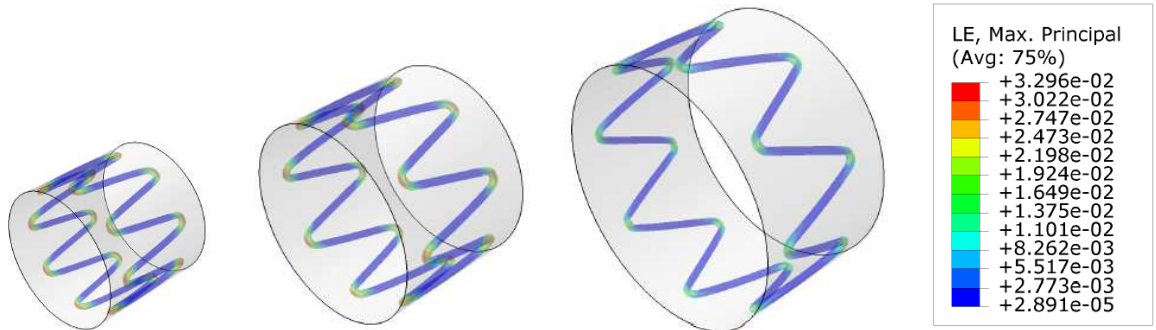


Figure 3.11: Deployment analysis steps with logarithmic strain values.

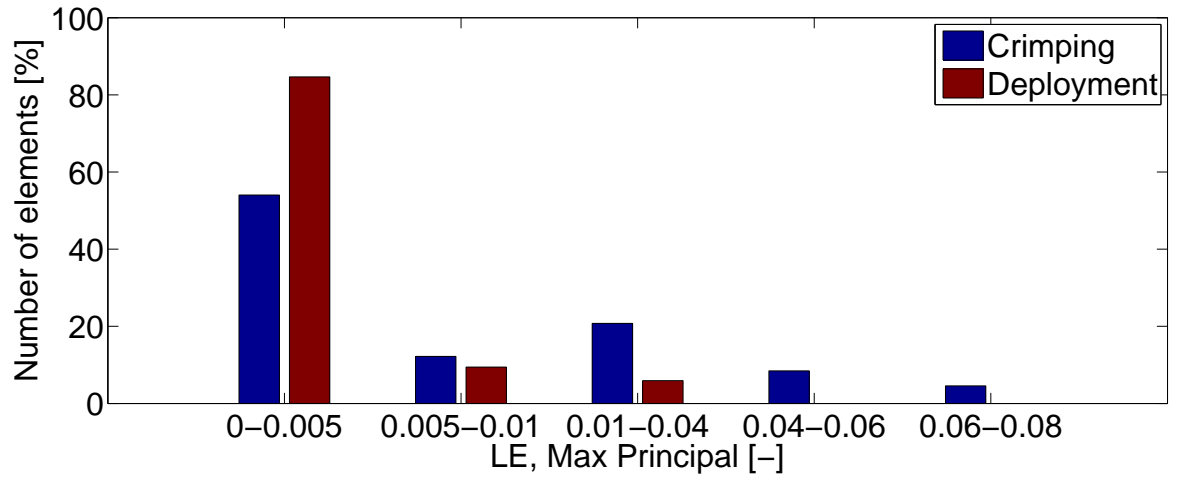


Figure 3.12: Histogram of logarithmic max. principal strain distribution during crimping step and deployment step, compared to number of elements which have those strain values in 8 characteristic integration points for each element. The strain values are plotted as the mean for each integration point and are calculated in MPa units. The number of elements are normalised respect with maximum number of elements.

Chapter 4

Medical imaging analysis and processing

In our study we focus on patient-specific simulation. The patient studied is a 74-year-old female, presented with an asymptomatic 5.5 cm pseudoaneurysm at the level of the distal anastomosis, 8 yr after ascending aortic repair for aneurysm; medical history included hypertension and atrial fibrillation. Because the patient declined a new sternotomy and the anatomy of the lesion was suitable, endovascular exclusion of the pseudoaneurysm was planned, with the use of a custom-made stentgraft (Bolton Medical Inc., Sunrise, Florida, USA). In order to compare the simulation prediction with the post-operative reality, as said in chapter 3, we need the 3D graft-aorta simulation after the implantation procedure.

Next step is to perform various operations with analysis of 4D CT images, which are necessary to extract the single ring from the CT (*segmentation*) and to match the reference system of the undeformed model with the reference system of the implanted ring (*registration*), we tried to deform the undeformed model reproducing the deformation of the implanted stent.

4.1 Images set-up

Post-operative CT images have been collected for research purposes, prior informed consent, thanks to IRCCS San Donato polyclinic hospital (Milan)[12]. The images were acquired with equipment 64-slice CT with Siemens Definition, with bolus of contrast agent concentration to 400 mg/iodine. The capture window high dose from 30% to 70% of the RR interval of the cardiac cycle. We used 20 post-processing DICOM CT images from patient with the following characteristics:

- dimension: $x=512\text{mm}$, $y=512\text{mm}$, $z=317\text{mm}$;

- voxel spacing: $x=0.6191\text{mm}$, $y=0.6191\text{mm}$, $z=1\text{mm}$;
- intensity range: min -1024, max 3071 HU;
- slice thickness: 1mm;
- best diastole: 67% with a thickness of 0.65 mm
- best systole: 33% with a thickness of 0.65 mm

4.2 Image segmentation

Segmentation [18] of medical images is the task of partitioning the data into contiguous regions representing individual anatomical objects. This task plays a vital role in many biomedical imaging applications: the quantifications of tissue volumes, diagnosis, localization of pathology, study of anatomical structure, treatment planning, partial volume correction of functional imaging data, and computer-integrated surgery. The goal of segmentation is to simplify and/or change the representation of an image into something that is more meaningful and easier to analyse. Image segmentation is typically used to locate objects and boundaries (lines, curves, etc.) in images. More precisely, image segmentation is the process of assigning a label to every pixel in an image such that pixels with the same label share certain visual characteristics. The result of image segmentation is a set of segments that collectively cover the entire image, or a set of contours extracted from the image. Each of the pixels in a region are similar with respect to some characteristic or computed property, such as colour, intensity, or texture. Adjacent regions are significantly different with respect to the same characteristics. The image partitioning level depends of the problem considered and segmentation should end when the object of interest has been found. From a practical point of view and in relation to our objectives, we can divide the segmentation procedures in the following categories:

- **Manual segmentation:** plan to manually draw the outline of the image portion you want to assign a specific label.
- **Automatic segmentation:** automatically divide the image into regions that show similar characteristics to them and differ from each other for the same characteristics. This type of segmentation is typically based on algorithms able to partition the image into a number of sets.
- **Semi-automatic segmentation:** represent a compromise between the two previous techniques. In this approach requires a modest interaction with the user, which is required to set some parameters of the algorithm. In this case, to solve our problem, it

is necessary use an automatic segmentation for preliminary steps, to extract the vessel part in which the stent is. After that, by using the manual segmentation, it is possible separate and segment the endograft, without vessel.

In literature there are described many software enabling the semi-automatic segmentation, but the one used in our work is the ITK-Snap software, described below [21].

4.2.1 ITK-Snap software

ITK-Snap (<http://www.itksnap.org>) is an open source software that allows you to perform manual and semi-automatic segmentation of anatomical structures from medical images with three-dimensional content. The segmentation is performed by active contours method and the setting of parameters is facilitated by a dedicated user interface. It is possible to perform manual segmentation of images by a contours tracking tool of the regions to be segmented. The main interface, show in figure 4.1, is intuitive and easy to use. It was, in fact, the intention of the developers making software that was easy to use even for users that do not belong to the branch of engineering. The interface allows the visualization of the axial images and sagittal and coronal reconstructions: a fourth window allows we to view 3D reconstruction at the end of the segmentation. On the left side of the interface, a series of toolboxes allow we to interact with the images and execute both manual and semi-automatic segmentation, whose procedures are explained briefly below.

Manual segmentation

For each slice of the stack containing the structure of interest, you perform the following steps:

- It outlines the contour of the structure to be segmented. The contour must necessarily be closed.
- It accepts the contours: all pixels inside the contours are labelled.

After performing the above steps on all slices, we can run the volume rendering of the anatomical structure, by a surface-based techniques that realised the extraction of geometric information from volumetric data, result of the segmentation process. Each segmented body, can be exported individually as a surface mesh in .stl format. A feature that has made ITK-Snap optimal also for the objectives of this work, as will be discussed later. This allows to interact with each frame as a separate, also giving the opportunity to perform volumetric calculations.

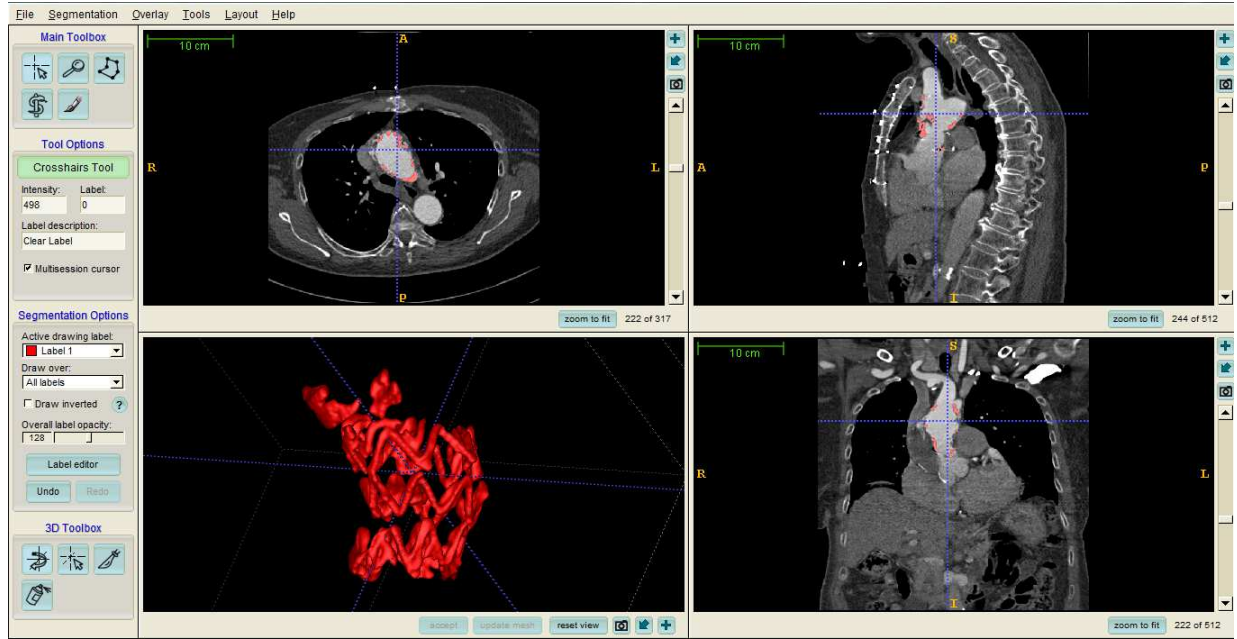


Figure 4.1: ITK Snap software interface. Viewing of segmented TAC images. In the window in the lower left Endograft volume rendering.

Semi-automatic segmentation

The software allows to perform even the semi-automatic segmentation, through a wizard. The following pictures are the steps of the procedure for the semi-automatic segmentation of the aortic endograft, object of study in this thesis. The first step is to define a ROI (*Region of Interest*), which encloses the structure to be segmented (see Figure 4.2). Next, the user must choose between two different realization way of a *feature image*, which is an image that contains the characteristics of the original image to be used to guide the segmentation algorithm.

- **Intensity regions.** Is based on the pixels intensity. In this case the user must properly set the parameters of a thresholding function through a special interface, as shown in figure 4.3. The operation is carried out interactively, allowing the user to verify the coverage of the area to be segmented. The parameters of the function must be set so that in the feature image is assigned a positive value to all the pixels belonging to the structure to be segmented, and a negative to the others.
- **Images edges.** Is based on the image edges definition. In this case the user must properly set the parameters function that allows to determine which intensity it is necessary to use for the structure contours. The function will be applied to the gradient image, in which they highlighted the edges of the structures. The feature image, in this

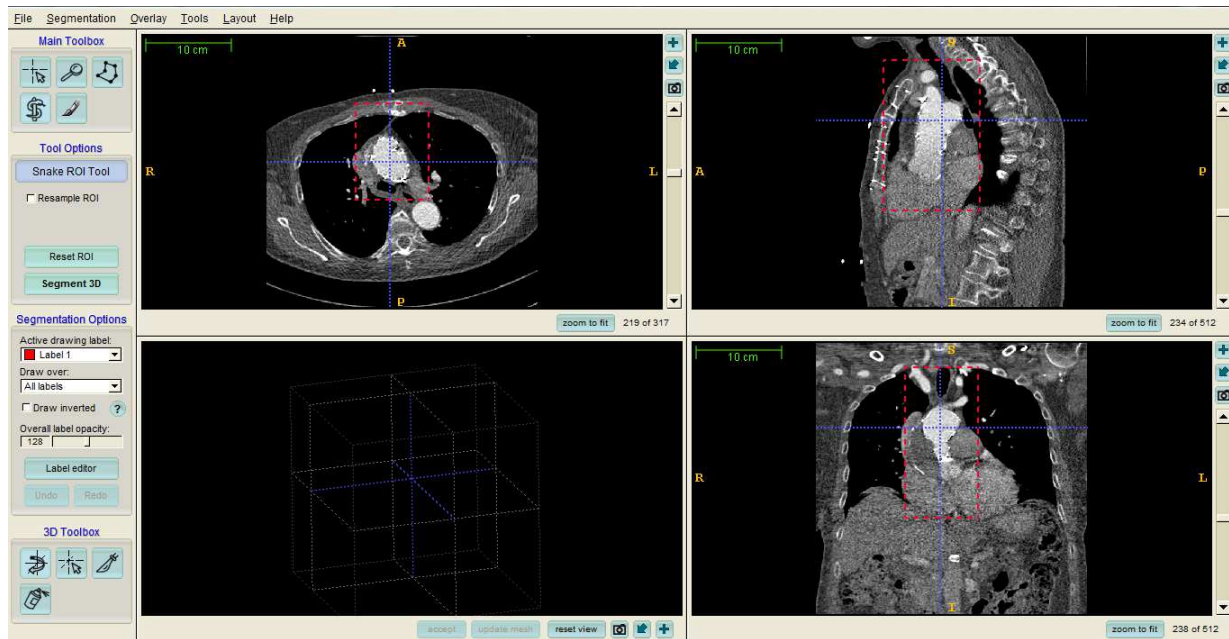
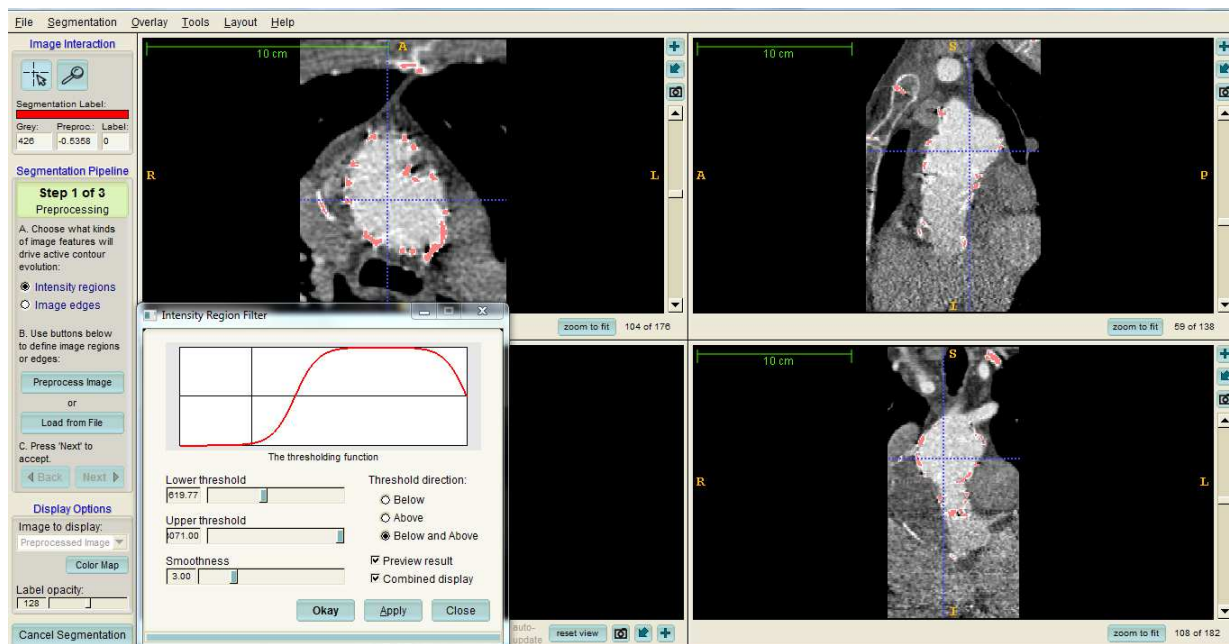


Figure 4.2: ROI definition for endograft segmentation.

case, assigns value close to 0 to the pixels of similar intensity to that of the edges of the structure, and values close to 1 to the pixels to the regions of uniform intensity. In this case it was important to exact only endograft pixels among the aorta surface.

Figure 4.3: Pre-processing of the image based on the *intensity regions*.

Next, the user must place one or more *seeds* within the region to be segmented as show in figure 4.4. These seeds are the starting point of the evolution of the segmentation algorithm, guided by the image features made with one of the previous methods. The algorithm evolves

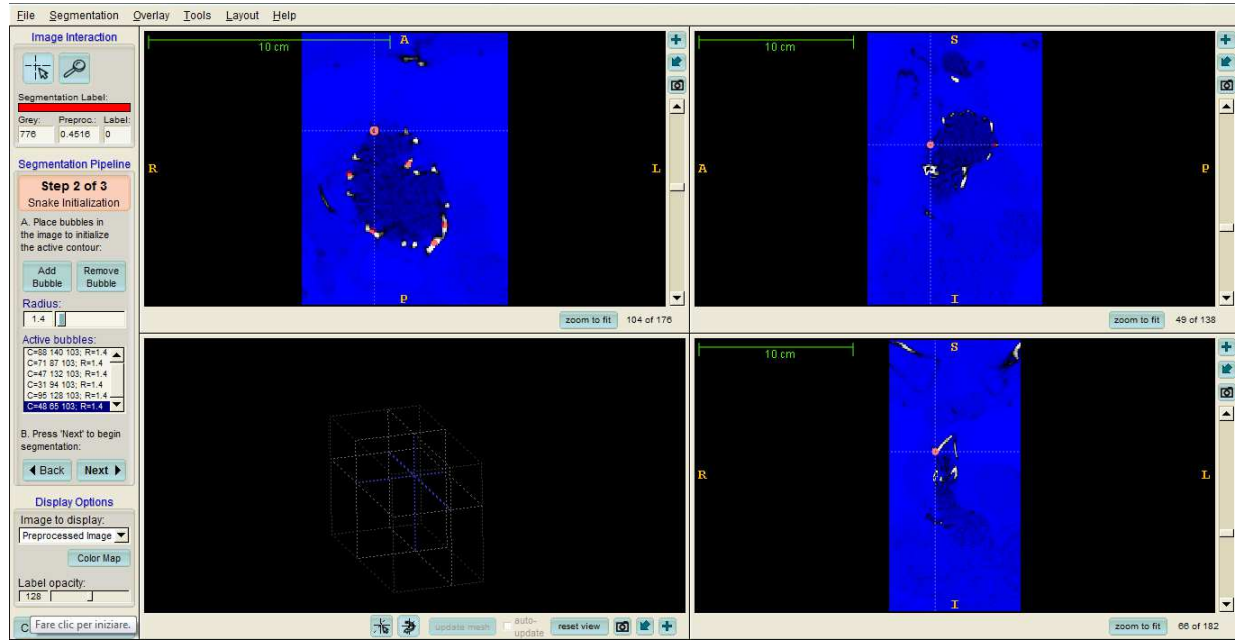


Figure 4.4: Arrangement of seed within the area to be segmented.

in three dimensions, as long as the user does not stop the process manually (the algorithm does not, in fact, a stopping criterion): the user can control the parameters of evolution, even if it requires an accurate knowledge of the mathematics behind the algorithm. The algorithm implemented in the original version of the software is based on the segmentation 3D method called *active contours*, in which the structure to be segmented is identified by one or more contours that evolve over time. The segmentation results is show in the figure 4.5.

Regarding our analysis, we focused mainly on the central ring of the stent. The information obtained from it can be subsequently extended to all rings of the stent, due to the modularity of the components. For this reason, as we can see in figure 4.6, the next step concerns the central ring extraction from the images segmented of the entire stent.

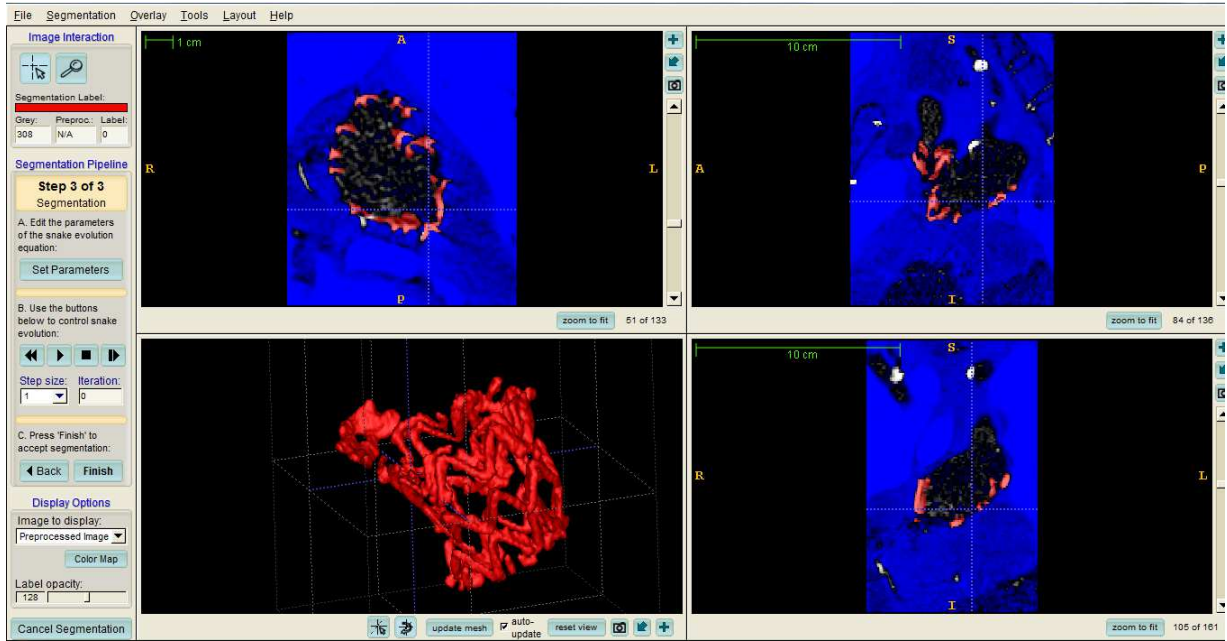


Figure 4.5: Segmentation results.

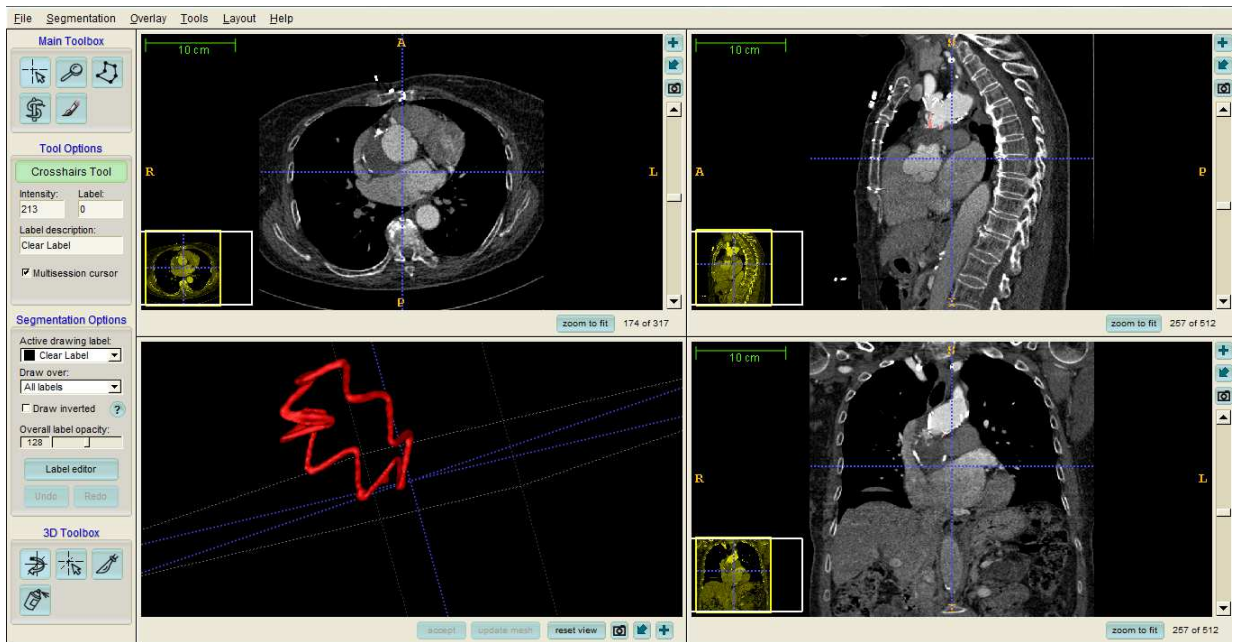


Figure 4.6: Extraction of stent central ring from image segmented.

4.3 CT images registration and centerline extraction

The main goal of this section is to get the CT image registered with respect to the central ring model and the centerline of central ring, for each frame, starting from the segmented and

registered image. To get the centerline data is important to calculate the deformed model from CT images and compare results. This can be accomplished through the use of a software called *VMTK*.

4.3.1 VMTK: The tool

VMTK (<http://www.vmtk.org/>) is a collection of libraries and tools for 3D reconstruction, geometric analysis, mesh generation and surface data analysis for image-based modelling of blood vessels. Born as a result of Luca Antiga's post-doc time at Robert Research Institute in 2003, continued through several years, with a few development bursts along the way. *VMTK* is composed:

- C++ classes (VTK and ITK -based algorithms)
- Python classes (high-level functionality - each class is a script). Python is a programming language that lets you work more quickly and integrate your systems more effectively.
- PypeS - Python pipe-able scripts, a framework which enables *VMTK* scripts to interact with each other.

In this work *VMTK* is used for geometric analysis, and in particular, to register CT images and simulation model and to compute the centerline from the ring.

CT Images Registration

The next goal is to match the reference system of the Abaqus model, with the reference system of the CT images. In order to make this transformation it is necessary to use the *VMTK* Registration tool. For simplicity we go to apply a roto-translation to CT images, in such a way as to bring their reference system, with the coordinate system of the model in Abaqus. The command line we used to register a surface to a reference surface using the ICP algorithm is: *vmtkicpregistration -ifile FRAME.stl -ofile FRAME icp.stl -rfile SIM.stl* where:

- *SIM.stl* is the reference surface, modelled by Abaqus.
- *FRAME .stl* is the input surface, before registration.
- *FRAME icp.stl* is the output registered surface.

The ICP (Iterative Closest Point) algorithm match two surfaces. The core of the algorithm is to match each vertex in one surface with the closest surface point on the other, then apply the transformation that modify one surface to best match the other (in a least square sense). This has to be iterated to get proper convergence of the surfaces. In figure 4.7 we can see the registration result. To read more about ICP see the appendix A.

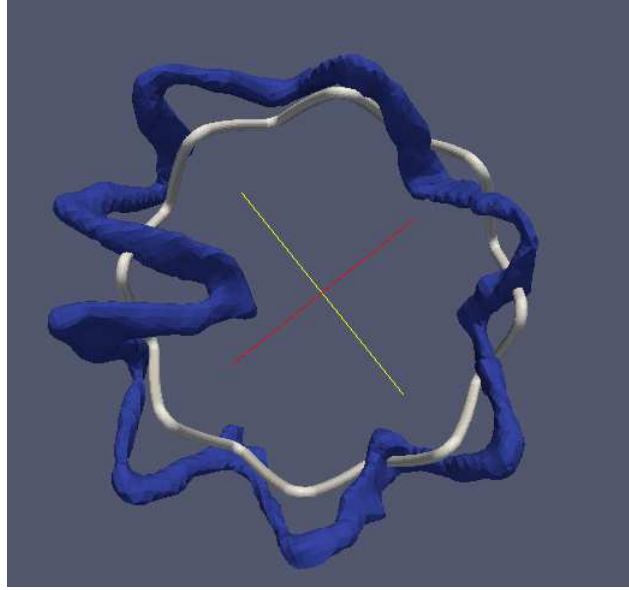


Figure 4.7: Result of ICP registration between the undeformed model (white) and CT image (blue).

Centerlines extraction

Centerlines are powerful descriptors of the shape of vessels, or stent, in this case. Although the concept of what a centerline is more or less intuitive, their mathematical definition is not unique. A lot of methods have been proposed in the literature for the computation of centerlines both from angiographic images and 3D models. The algorithm implemented in *vmrk* deals with the computation of centerlines starting from surface models, and has the advantage that it is well characterized mathematically and quite stable to perturbations on the surface. Briefly, centerlines are determined as weighted shortest paths traced between two extremal points. In order to ensure that the final lines are in fact central, the paths cannot lie anywhere in space, but are bound to run on the Voronoi diagram of the vessel model. There is a huge literature on Voronoi diagrams, however, as a first approximation, we can consider it as the place where the centres of maximal inscribed spheres are defined. A sphere inscribed in an object is said to be maximal when there is no other inscribed sphere that contains it. So, for every point belonging to the Voronoi diagram, there is a sphere centred in that point that is a maximal inscribed sphere (the information relative to the radius is therefore defined everywhere on the Voronoi diagram). Centerlines are determined as the paths defined on Voronoi diagram sheets that minimize the integral of the radius of maximal inscribed spheres along the path, which is equivalent to finding the shortest paths in the radius metric. The way this is done is by propagating a wave from a source point (one endpoint of the centerline)

using the inverse of the radius as the wave speed and recording the wave arrival time on all the points of the Voronoi diagram, and then backtracking the line from a target point (the other endpoint of the centerline) down along the gradient of arrival times. The script that allows to compute centerlines in *vmtk* is: *vmtkcenterlines*. It takes in input a surface and spits out centerlines, the Voronoi diagram and its dual, the Delaunay tessellation (or, better, the subset of the Delaunay tessellation internal to the surface).

The command to calculate the centerlines of central ring, for each frame, is: *vmtkcenterlines -ifileFRAME.stl -ofileFRAMEcl.vtp* A render window will pop up, asking to specify points on the surface that will act as source points. At the end, we will have our centerline, as we can see in fig. We can look at the results in this way: *vmtksurfacereader*

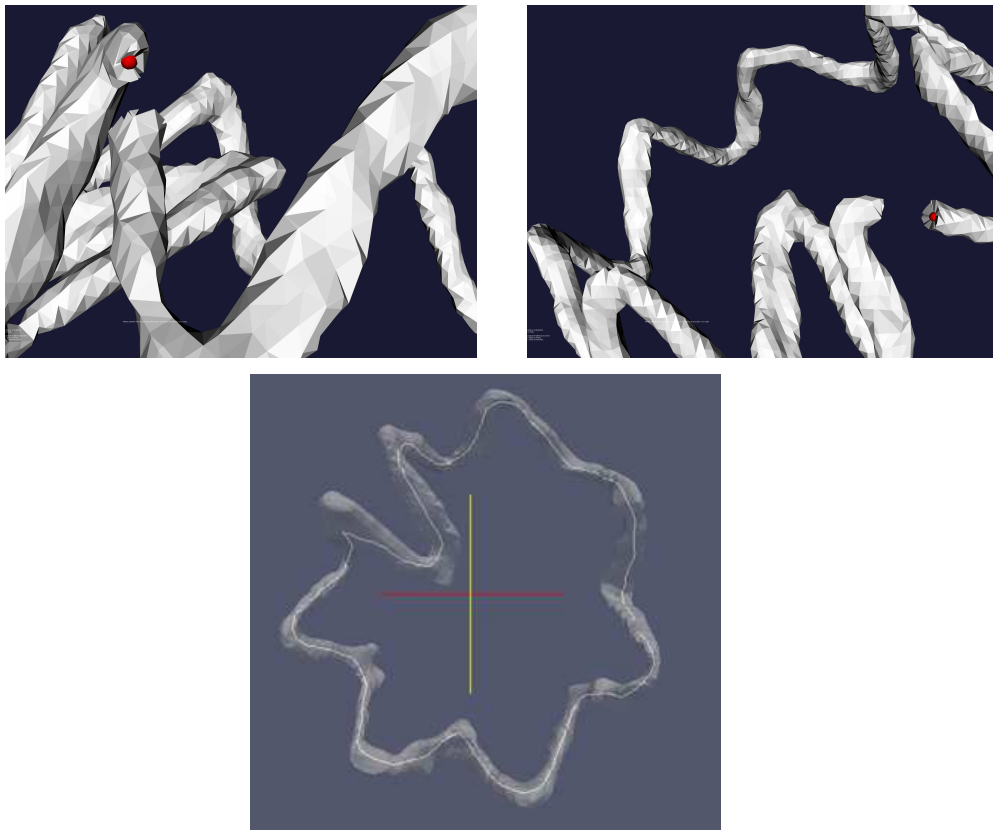


Figure 4.8: VMTK centerline reconstruction.

-ifileFRAME.stl--pipevmtkcenterlines--pipevmtkrenderer--pipevmtksurfaceviewer--opacity0.25 Before to do that, it is necessary to open the structure. This is possible thanks an other open source software called *Paraview*. ParaView (<http://www.paraview.org>) is an open source multiple-platform application for interactive, scientific visualization. It is an application built on top of the Visualization Tool Kit (VTK) libraries. Paraview allows the visualization of three-dimensional geometries and the execution of a large number of analysis

through the use of filters, some already present in the software and executable by the tools bar, others imported from the outside, and still others created manually within the software.

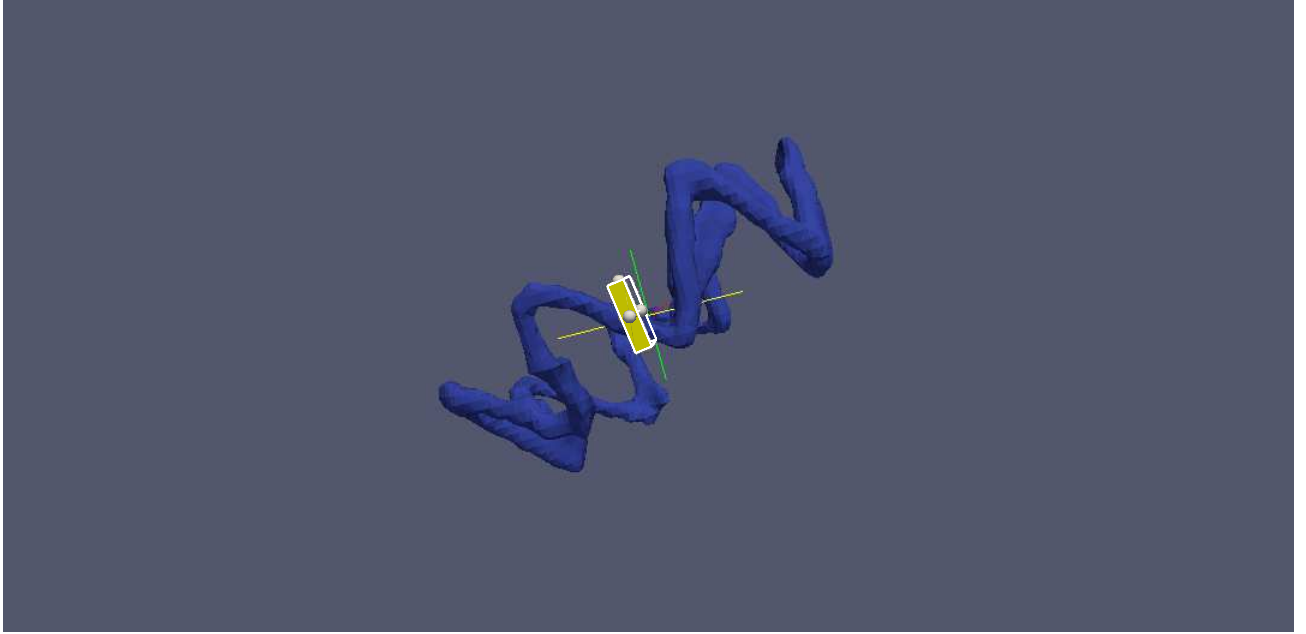


Figure 4.9: Clip filter applied to the ring using Paraview.

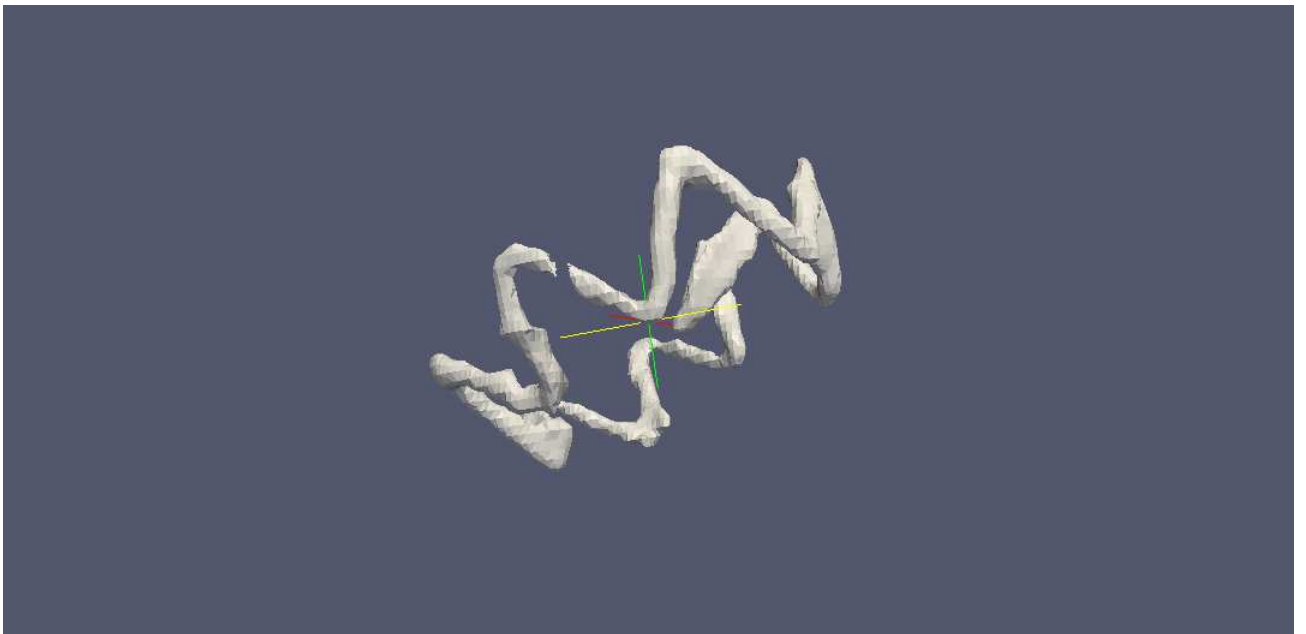


Figure 4.10: Opened structure after Paraview manipulation .

4.4 Results

4.5 Endoprosthesis dynamics: real implanted device

Analysing the CT images processed in 20 different time instants, it is possible to evaluate the movements of the stent, during time. An interesting evaluation can be considered comparing the first frame with the others and analysing how the distance between frames changes. In this case we can see in figure 4.11 that the distance from first frame to fourth and five frames is maximum, also compared with systolic peak. We can also compare graphic with characteristic

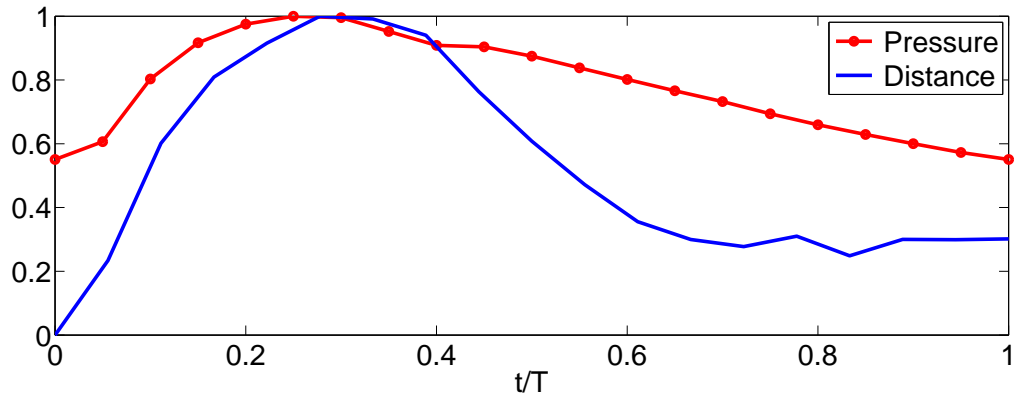


Figure 4.11: In this graphic we compare the distance between first frame and the others from CT images with characteristic systolic curve (the first frame with the second, the first with the third frame and so on) to see if there is a correlation between the two curves. The x axis represent the normalised time and y axis has normalised pressure from a characteristic systolic curve in healthy patient, compared to normalised distance of the stent during different frames.

systolic curve, to see that in correspondence of the systolic peak we have the smallest distance between the frames as we can see in figure 4.12. An interesting evaluation is to see if frames are all necessary to analyse stent kinematics during cardiac circle. In the figure we emphasized the frames that have a higher variability and which constitute the most important frames for the analysis of the kinematics of the implanted device.

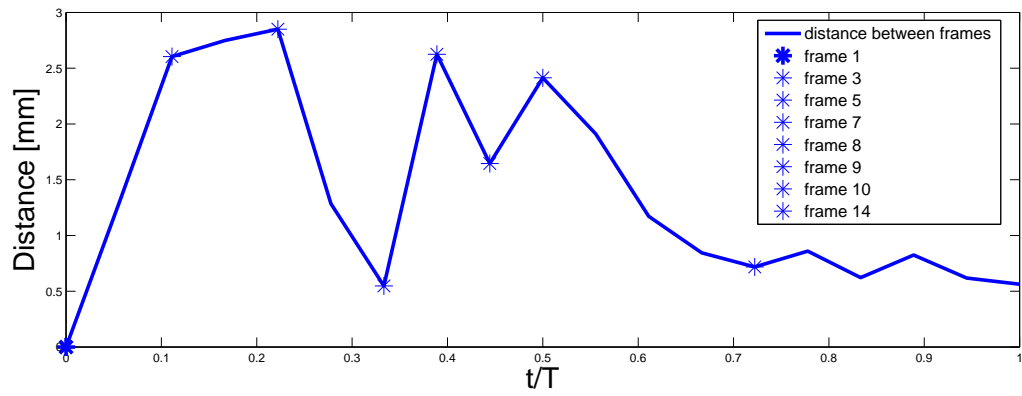


Figure 4.12: In this graphic we compare the distance between frames couples from CT images (the first frame with the second, the second with the third and so on) to see if there is a particular trend. The x axis represent the normalised time and y axis represents the distance of the configurations of the stent in different time instants.

Chapter 5

Numerical and qualitative results

In this chapter, we proposed an alternative approach compared to the standard analysis, based on the boundary conditions imposed on the central nodes of the stent. Then we will compare the results obtained in the two cases. To reproduce the real behaviour of the stent from the CT images, an another approach was developed.

5.1 First approach: centerline analysis

An other used method to evaluate stress and strain values is to pass from undeformed model configuration to first time instant CT images configuration applying boundary condition, obtained from catheter analysis, only to central ring nodes. Before to do this step is necessary to use the approach with a small stent part, and after to extend the procedure to entire ring. The used software is Abaqus Standard.

5.1.1 Preliminary steps of work

By considering the initial stent configuration, without applied loads, the first goal is to determine labels and coordinates of centerline nodes. This step is effected by using the wire curve (2D), from which the stent is built. From the stent portion, through a simple script in Matlab, it is possible to derive the coordinates of the nodes and the labels of the central curve.

The Matlab script works loading two documents .txt.; the first one with wire nodes and the other with the solid stent nodes. The script calculates the difference of nodes coordinates from the wire curve and from the stent, and select only the nodes that have the minimum distance between them. These nodes selected represent the central nodes of the stent.

After that, central nodes of a stent portion were determined and a deformation analysis was performed. At the end of the analysis we had the central nodes of the stent before and after the application of loads. The difference of the coordinates of the nodes before and after



Figure 5.1: ABAQUS. Central nodes of stent

the analysis, allows to define the displacement of the central nodes.

To verify the correctness of the model, the displacement values previously calculated were used as boundary conditions (BCs) and applied only to central nodes of the stent in the initial configuration, undeformed, with the goal of finding the configuration deformed. As show in figure 5.3 the results of the two analysis are perfectly comparable and similar. As expected the values of Von Mises stress are different because in the first case, the boundary conditions were applied only to the central nodes, while in the second figure the load was applied to the entire structure. After working with small stent portion, next goal was to consider the stent

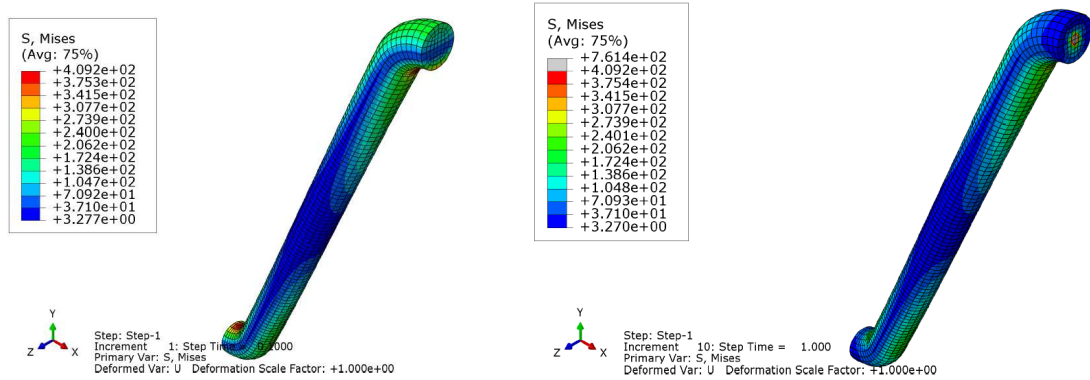


Figure 5.2: ABAQUS. von Mises stress calculated by applying a deformation analysis at initial configuration of stent(a) and by applying BCs of central nodes(b). The stress values represent the interval values assumed by the model during the analysis..

as formed by its repeated equal portions. In figure 5.4 we can see the planar stent and 3D stent representation. With the same procedure used for a stent portion, we found the central nodes (coordinates and labels), both for planar and rolled stent. T

To verify the von Mises and displacement values accuracy, we calculated the error between the

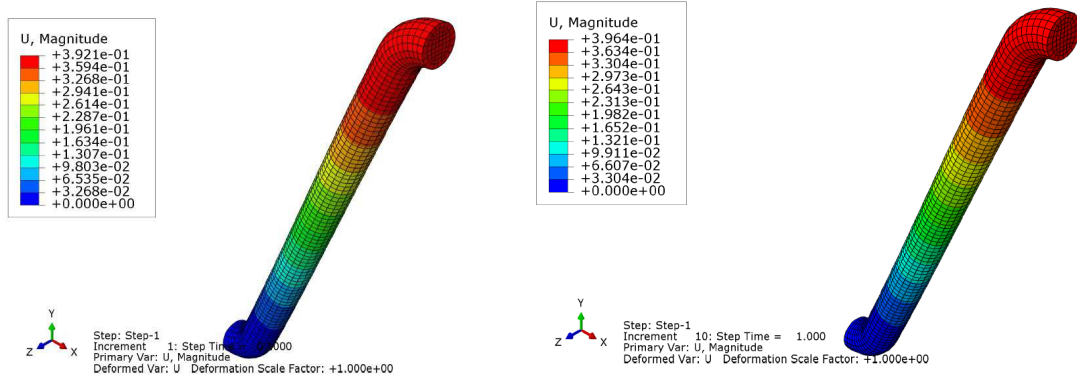


Figure 5.3: ABAQUS. Displacement calculated by applying a deformation analysis at initial configuration of stent (a) and by applying BCs of central nodes (b). The displacement values represent the interval values assumed by the model during the analysis.

results obtained by applying a deformation analysis at initial stent configuration compared with others obtained by applying central nodes boundary conditions. In this analysis we decided to save 10 values of stress and strain evenly distributed over the time interval in which the analysis is carried out and only these 10 values were compared, as we can see in the following table 5.1.

Frame number	Error values
1	0,000006156
2	0,000012491
3	0,0000191
4	0,000029165
5	0,000037729
6	0,0000465
7	0,0000557
8	0,0000646
9	0,000073207
10	0,000080965

Table 5.1: Error values.

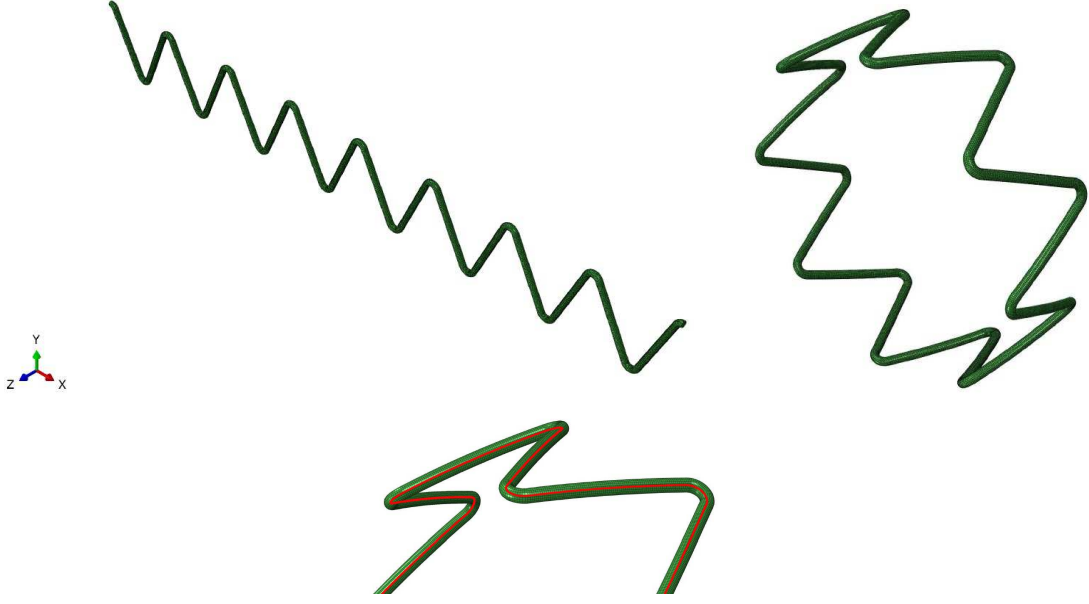


Figure 5.4: Planar stent, 3D stent representation and central nodes set of 3D stent configuration.

5.1.2 Simulation strategy: from undeformed model to crimping and deployment state

Starting from previously results, next step is to reproduce the same stress and strain values obtained by catheter displacement control analysis and impose them on wire centerline. Through Abaqus it is possible to obtain as output displacement values calculated for all ring nodes at specific time instant. By using a script in Matlab we derived the displacements coordinates only for the wire centerline nodes and we used them as boundary conditions to those nodes. To create a new input file with displacement applied to central nodes, every time instant frame output is an input step for the next analysis. The goal is to obtain similar results in the two analysis by applying boundary conditions only on the wire centerline, without using catheter. This strategy is necessary because we have only post-operative CT images with the device positioned in loco and partially crimped, so the only informations we can use to compare results, and to work on, is the endograft centerline and the contact with catheter. The crimping and deployment analysis step are shown below: As we can see in figure 3.8 and 5.5 the maximum von Mises stress values are similar.

5.1.3 Crimping: comparison between stress and strain values

As said before, crimping state is one with highest stress values, due to is considerable reduction in diameter. In this case is interesting evaluate the stent stress and strain condition even

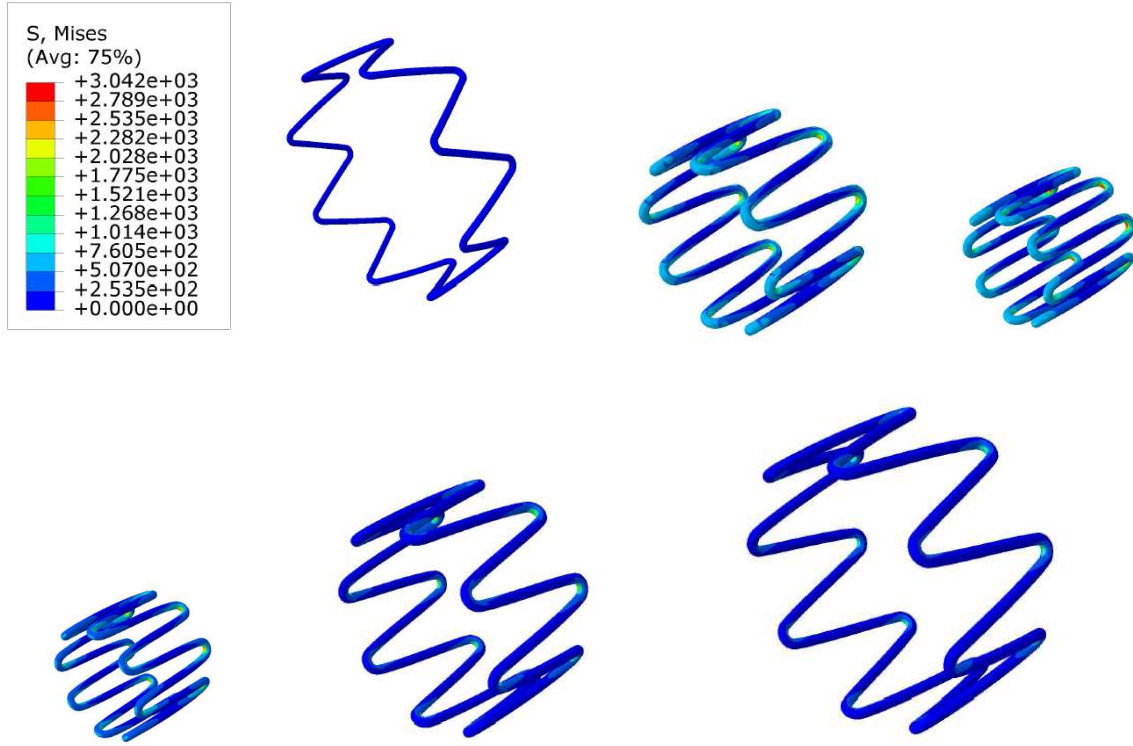


Figure 5.5: Crimping and deployment analysis steps by applying Boundary conditions to wire centerline (left to right, up to down). The stress values represent the interval values assumed by the model during the analysis.

before the release of the device in the patient. We can analyse the differences between the two approaches: use of rigid surface as catheter to induce the stent diameter variation, and the other one obtained with displacement boundary conditions applied to central nodes of the ring. As we can see in figure 5.6, this is the step with highest von mises stress values, due to

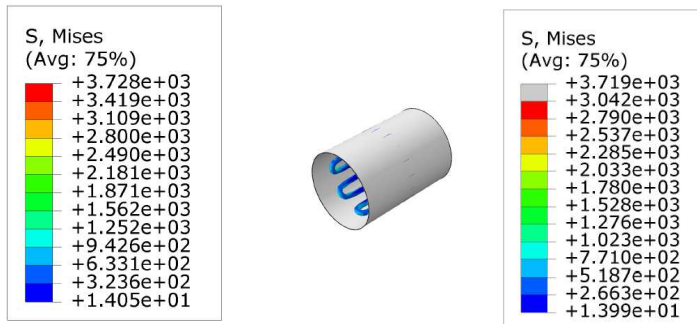


Figure 5.6: Von Mises stress values during crimping analysis with two approaches.

strong stent diameter reduction inside the catheter. The highest stress value (3.728 GPa in

analysis with catheter and 3.719 GPa in the other one) is the same in the two analysis, but is referred to few nodes with respect the total. So in the same analysis conditions (geometry, materials, mesh) we can use both in the same way to have the same results. We also analysed logarithmic strain values (LE Max.Principal) to evaluate if, in this case either, it is possible compare results of two approaches. As show in figure 5.7 the LE results are similar in the two cases. This leads us to think that getting expected results using one or the other method is nearly equivalent.

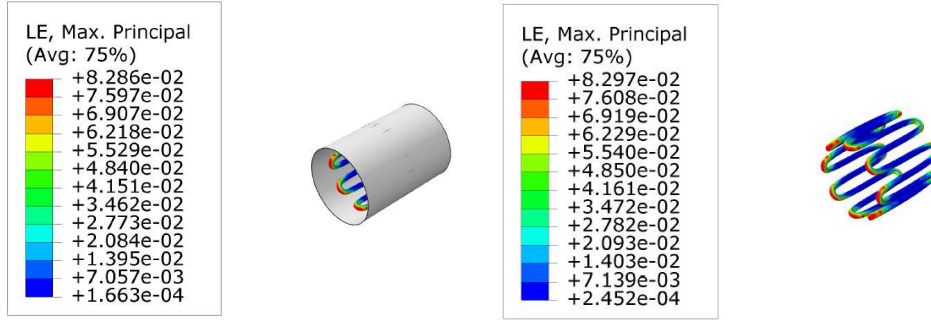


Figure 5.7: Logarithmic strain values during crimping analysis with two approaches.

5.1.4 Deployment:comparison between stress and strain values

Deployment state is another critical step associated with the release in the aneurysm of the self-expandable stent. In this case either, we evaluate von mises stress and logarithmic strain to compare results from two approaches used in the stent kinematics analysis. In this case

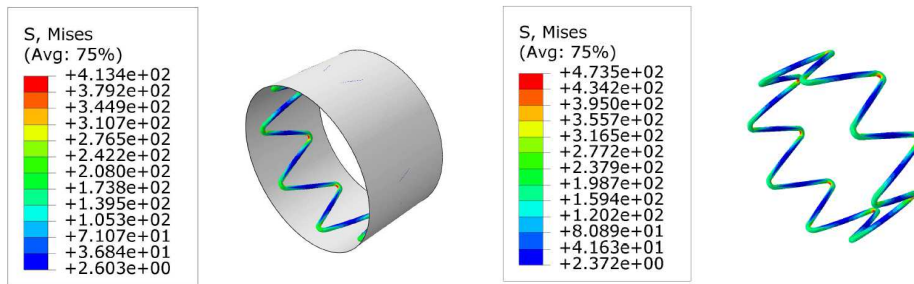


Figure 5.8: Von Mises stress values during deployment analysis with two approaches.

both, the values of stress that those of strain, are similar, as previously. For von mises stress the smallest value is the same in both analysis (2.603 MPa for catheter case and 2.372 MPa for centerline analysis), the highest stress values is present in analysis without contact respect with catheter analysis (413.4 MPa in the left figure and 473.5 MPa in the right figure).

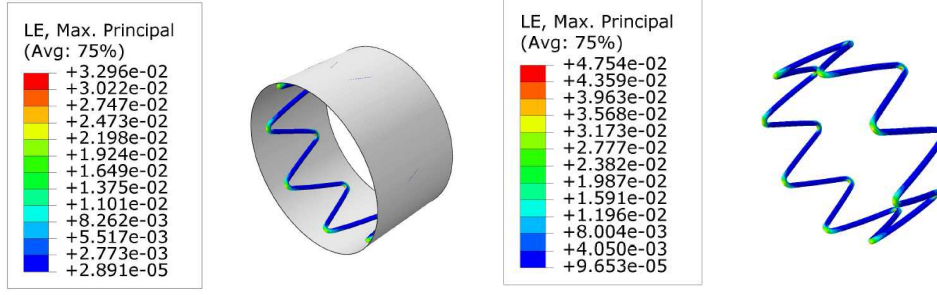


Figure 5.9: Logarithmic strain values during crimping analysis with two approaches.

For logarithmic strain is the same situation seen for stress values. This difference in values in the two cases may be due to the application of displacements to the central nodes that implies a greater stress condition of particular regions. This is demonstrated analysing the most stressed regions in figure 5.10. In general the ring is more stressed in catheter analysis, because of deformation imposition by catheter, but the stress values are highest in specific regions of the ring in the second analysis. In literature Keinstreuer et al. [6] found comparable

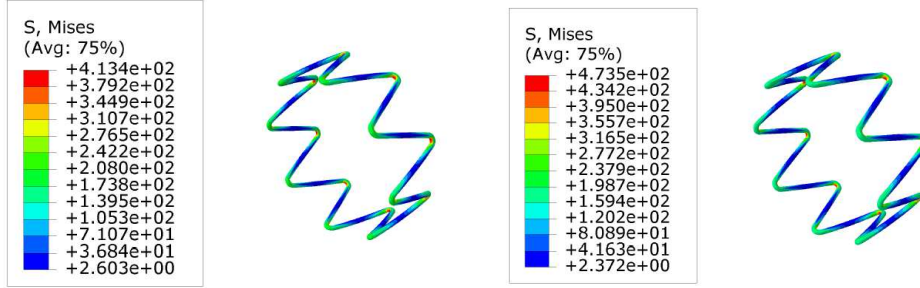


Figure 5.10: Von mises stress distribution in catheter analysis (left) and centerline analysis (right).

logarithmic strain values with respect our study, while von mises stress values are highest in our work, with respect the paper.

We tried to apply displacements to the nodes of the centerline of the ring in order to induce the displacement of the stent from the undeformed configuration to the first frame deformed configuration, but this still represents a limitation of this approach as a possible future development. So we developed another approach to evaluate the stress induced in these devices. The method is explained below.

5.2 Second approach: catheter analysis

The analysis made during the study were implemented with Abaqus Standard, as said in 3.2.2. In this section we tried to pass from the stent configuration released in the artery, to deformed configuration of the first CT image. The problem is highly non-linear, with large displacements and deformations and Abaqus Standard do not assure the analysis convergence. For this reason we tried to run this analysis with Abaqus Explicit. The difference between two methods are described in section 3.2. Abaqus explicit does not require the simultaneous solving of an equations system or the calculation of a global stiffness matrix. Instead, the solution is advanced kinematically from one increment to the next. The deformation of the stent is induced by the deformation of the rigid surface thanks to the contact between the two. As said before, analysis by the contact is an extremely delicate analysis which guarantee the convergence only for particular values of the parameters set (e.g, time step: 0.1).

5.2.1 Simulation strategy: from crimping to deformed state

One possible solution to evaluate stress and strain values from undeformed model to CT images is to create different rigid cylindrical surfaces:

- first surface: undeformed structure, figure 5.11 (a);
- second surface: crimped structure, figure 5.11 (b);
- third surface: deformed structure as first CT image, figure 5.11 (c) .

The analysis is divided in two step: the first step allows the passage of the stent from the undeformed configuration to the crimped configuration (diameter reduction) and the second step switches from the crimped to the deformed configuration of the first frame of the CT image. The deformation of the stent is determined applying a displacement control analysis to the undeformed cylinder, in which each node of the cylinder is associated with a displacement value given by the difference of nodes coordinates from undeformed cylinder to the crimped cylinder. In addition to the boundary conditions associated with the cylinder nodes, displacement/rotation boundary conditions are applied of lower nodes of the stent (we considered a node for each lower end of the stent), going to fix the value of theta in a cylindrical coordinate system, to avoid any rotation of the stent. In the second step we put also displacement/rotation boundary conditions to superior nodes of the stent with coordinates from the same labelled nodes in first deformed configuration. During second step of the analysis the upper nodes of the ring will bring exactly the same position of the upper nodes of the deformed configuration derived from CT images. In the figure 5.12 we can see the first CT image in

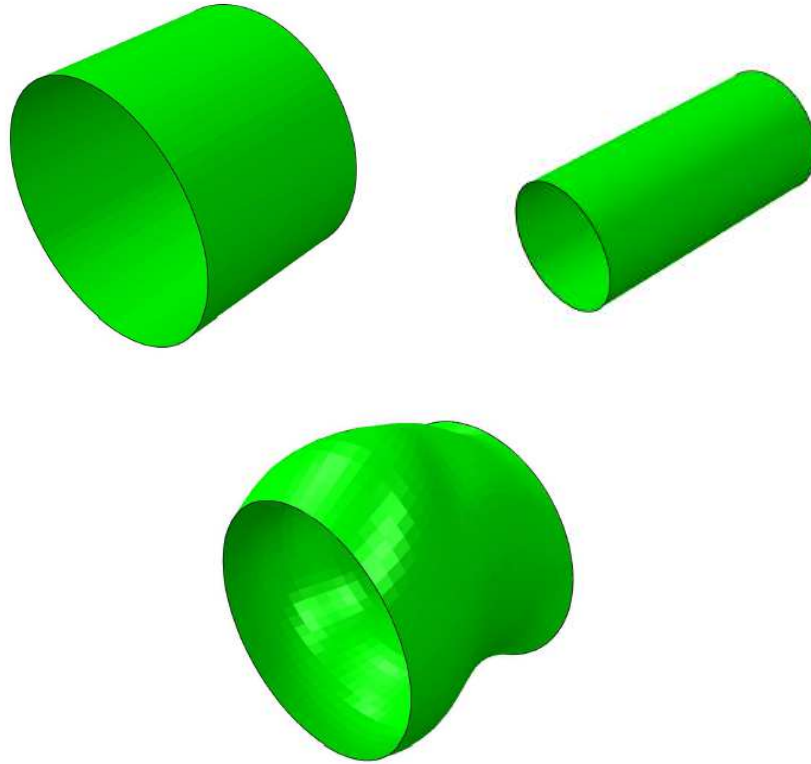


Figure 5.11: from left to right. Rigid surfaces used for contact analysis to deform the stent from undeformed configuration (a) to crimping configuration (b) and from crimping configuration to first CT image configuration (c).

which we highlighted lower nodes (black) and upper nodes (red). The coordinates of the nodes are extracted from the centerline of each frame previously calculated (section 4.3.1).

As shown in figure 5.13 during the analysis we pass from the condition of crimping in which the diameter of the stent is reduced, to the condition in which, by applying the coordinates values of the upper nodes of the first frame, the stent is deformed in such a way congruent to the real condition. Through these steps we obtained a good overlap of the released stent compared to deformed configuration. Despite this good overlap, by applying boundary conditions at the upper nodes we do not have a perfect match. To assess the accuracy of the results compared to the reality, we calculated the distance between the corresponding points in the two configurations (figure 5.14). As we can see in the figure, the regions of the stent, whose nodes have the greater distance with respect to the CT, are those in which there is the greatest deformation of the stent, which makes more difficult the overlap of two stents. The distance is calculated from VMTK software, 4.3.1 with the command: `vmtksurfacdistance -ifile SIM.stl`

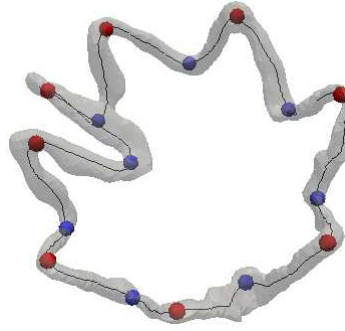


Figure 5.12: CT image considered for the deformation analysis of the stent. Upper nodes (red) and lower nodes (black) are highlighted. The lower nodes are blocked along theta cylindrical coordinate to avoid rotations, and to upper nodes we imposed, as boundary conditions, coordinates values from upper nodes of this frame.

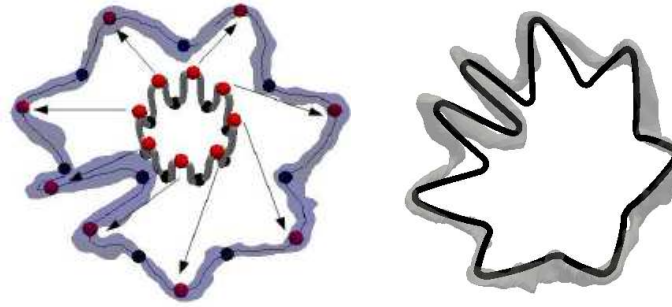


Figure 5.13: Crimping step and deformation step. Comparison between modelled stent and real implanted device. The arrows in the left image indicate how we moved the nodes of interest to go from the crimped configuration, the deformed configuration.

-rfile FRAME 1 icp.stl -ofile SIM dist.stl -distancearray DistanceArrayName. Where:

- SIM.stl: is the first surface reader;
- FRAME 1 icp.stl: is the second surface reader;
- SIM dist.stl: is the surface writer;
- distancearray DistanceArrayName: name of the array where the distance of the input surface to the reference surface has to be stored.

5.2.2 Stress and logarithmic strain results

In this section we analysed von mises stress and logarithmic strain at the end of the analysis, in deformed distribution. As we can see in figure 5.15, von Mises stress is greater in the regions

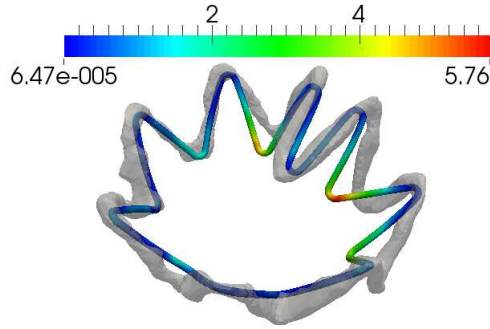


Figure 5.14: The image represents the distribution of the distance into the stent simulated, compared to the implanted stent after the analysis of contact. The highest values of distances are at the nodes more deformed stent, as expected. The distance is calculated in millimetre.

of the stent where there are bends and in particular the regions most stressed are those most deformed. This is demonstrated also in literature with several papers[10, 6, 25]. Regarding the values associated with the logarithmic strain (figure 5.16), the high strain locations are the curvatures of the stent [28, 23, 5], in particular, where is the highest deformation of the stent. We rescaled the values of stress and strain in order to make the result displayed, turning the quantitative analysis in a qualitative analysis of the results. We plotted stress and logarithmic strain values for crimping and deployment step. As we can see in the figure 5.17, the stress values associated with the deployment steps are lower compared to the values of the stress in crimping step, as we expected. The number of items associated with higher values of stress in crimping and deployment are comparable. The considerations can be made for logarithmic strain values, shown in figure 5.18. In this case the number of elements are higher for strain values in deployment step, for logarithmic strain values between 0 and 0.005.

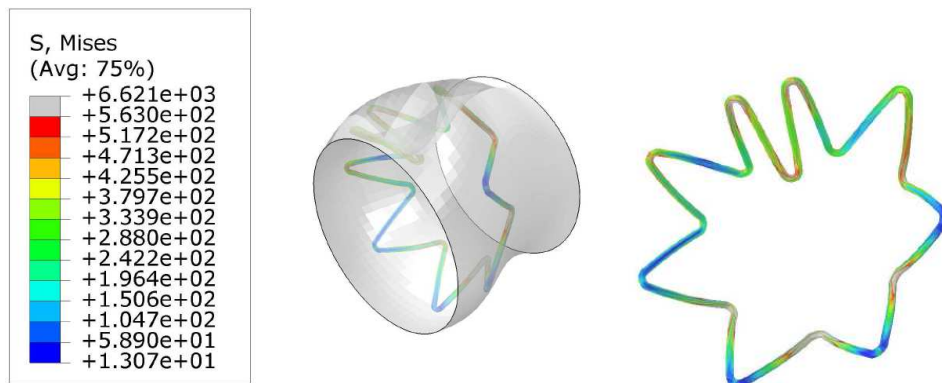


Figure 5.15: Von mises values calculated during the analysis. The stent figure is referred to the last frame of the second step. The values are calculated in MPa.

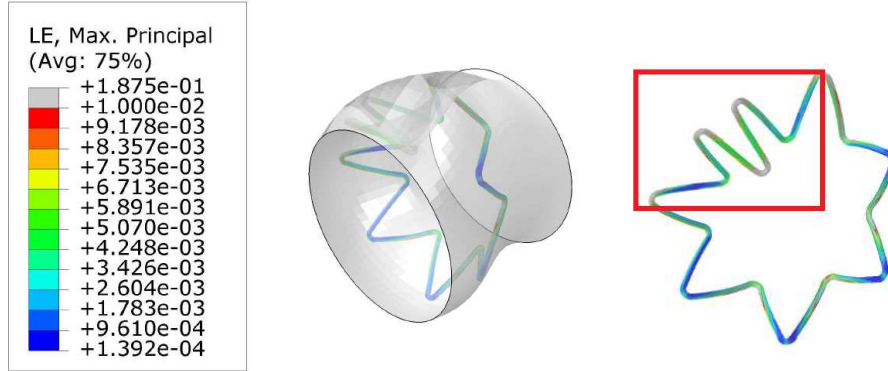


Figure 5.16: Logarithmic max principal strain calculated during the analysis. The stent figure is referred to the last frame of the second step. The values are calculated in millimetres. The red rectangle highlights the regions with a high value of deformation in the stent.

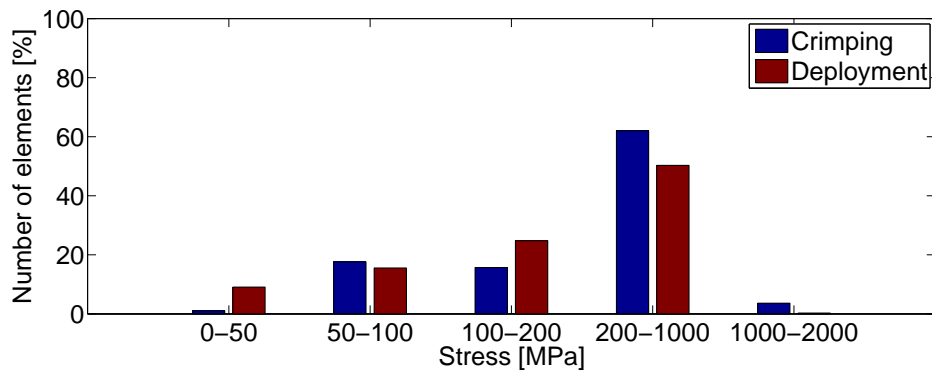


Figure 5.17: Histogram of von mises stress distribution during crimping step and deployment step, compared to number of elements which have those stress values in 8 characteristic integration points for each element. The stress values are plotted as the mean for each integration point and are calculated in MPa units. The number of elements are normalised respect with maximum number of elements.

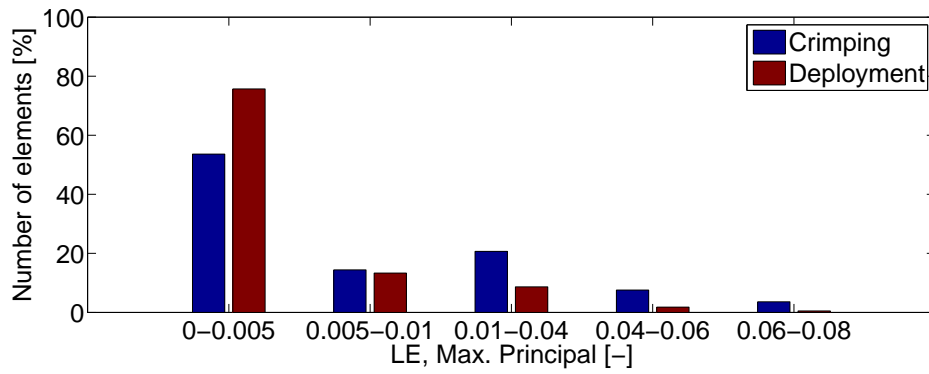


Figure 5.18: Histogram of logarithmic max. principal strain distribution during crimping step and deployment step, compared to number of elements which have those strain values in 8 characteristic integration points for each element. The strain values are plotted as the mean for each integration point and are calculated in MPa units. The number of elements are normalised respect with maximum number of elements.

Chapter 6

Conclusions

The present study focused primarily on a new technique for minimally invasive endovascular treatment of aortic aneurysms. The search for an optimal stent design occurred through finite element structural analysis which was able to evaluate device performance, such as von mises stress and logarithmic strain, to analysing the performances of implanted stent, during the cardiac cycle.

The study was developed from a specific clinical case, which referred to the EVAR procedure and presented an incorrect apposition of the stent. Starting from this condition, we tried to investigate set of variables that could provide information about the mechanical condition of the implanted stent. Since it is an approach born to treat abdominal aortic aneurysms, in order to extend its use in the thoracic and ascending aorta, is necessary to modify the design of the stent and make it congruent with the anatomical region in which it is placed. The information about those problems in literature are few and the standard approach used for the calculation of these variables provides the modelling of the stent and a rigid surface (simulating catheter) through an analysis using contact condition, which has allowed the development of dynamic crimping and deployment to which is normally encounter the stent before being inserted into the patient, and after its release in the vascular region.

It has been demonstrated that finite element analysis can be a valid method to investigate several aspects of stenting procedures, such crimping and deployment kinematics in stent simulation. Von mises stress and logarithmic strain analysed for this approach have comparable values from literature. Starting from these results we analysed the CT images of the patient in order to bring together the ideal case with the clinical reality. A preliminary analysis of CT images in relation to the cardiac characteristic curve showed an interesting correlation between the systolic peak and the maximum displacement of the stent during this peak. We have also seen that it is sufficient to consider only the frames that have a greater variation during the cardiac cycle in order to characterize the behaviour of the stent described above.

Through the analysis of medical images we brought the deformed configuration of the stent, achieved through finite element analysis, to the deformed configuration of the CT image in order to evaluate the performances of the stent in the real case.

The results analysis show that the deformation of the stent is not uniform, but depends on the anatomy in which the stent is inserted. Furthermore, by analysing the values of von Mises stress and logarithmic strain in the deformed configuration we noted that the points of highest stress are those in which the stent is bend, and in particular where it has reached the highest deformation. We tried to develop another approach based on displacements applied to the central nodes of the stent, relative to the centerline, in order to obtain the same results obtained through the analysis with the contact. This analysis has been developed for the two main steps (crimping and deployment) and we saw that the trends of the variables analysed were comparable with the standard analysis. The next step of this approach is to pass from released stent configuration into the aorta to the deformed CT image, with particular attention to use parameters that are likely to lead to the convergence of the method.

6.1 Limitations and future works

The study analysed in this thesis is an experimental approach to evaluate real medical and biomedical situations. Despite the preliminary results, there are many limitations that need to be studied in greater depth in each of their part and analysed in order to improve the overall outcome of the analysis.

The first concerns the used material for the stent realisation. We do not know the properties of the specific material used for the prosthesis. This represents a limitation to achieving the desired results, because we do not have the full knowledge of all of its properties and characteristics, it is more difficult to predict the mechanical behaviour. A possible future development would be to perform the analyses carried out with different materials from Nitinol, look for correlations or differences in behaviour and be able to correctly predict the outcome.

Another improvement concerns the methods of image segmentation. During the process of segmentation, it was possible to modify the result working pixel by pixel. Even if the implemented image processing step provided a good performance, the influence of the segmentation and registration methods is still not clear, and further investigations are required. In particular, we have to assess the impact of segmentation parameters on the final results of the simulation. The model design do not include the use of polyester coating, but the focus was only on the nitinol central ring. A possible future work is to develop the analysis with the complete model device in all its parts to see if some variable changes its values or if the model has a different mechanical behaviour. In addition, we analysed only the first frame of the twenty available.

A future development could be going to analyse the stress levels in all frames and make a qualitative analysis on the variation of Von mises stress and the logarithmic strain during time.

Appendix A

Iterative closest point algorithm (ICP)

The ICP algorithm (<http://www.wisegai.com/2012/11/07/what-is-icp-iterative-closestpoint>) is used to minimize the differences between two clouds of points of the same object from two different scans. The first step of the algorithm is to find correspondence between the points of two clouds, each of which is taken as reference and the other as the target, the figure can explain the concept. ICP algorithm is based on the assumption that the two closest points are also the corresponding closer where you plan to have the minimum Euclidean distance. Since $p(X, Y, Z)$ target point and $q(X, Y, Z)$ reference point, the Euclidean distance is defined as the segment joining the two points p and q according to the law:

$$d(p, q) = d(q, p) = \sqrt{(q_1 - p_1)^2 + (q_2 - p_2)^2 + \dots + (q_n - p_n)^2} = \sqrt{\sum_{i=0}^n ((q_i - p_i)^2)} \quad (\text{A.1})$$

At this point, found the corresponding points, less than approximations, we need to define the function to be minimized by the method of least squares. The target surfaces to be aligned properly will be translate and rotate and the transformation τ will be a function of roto-translation. Using the algebraic matrices, rotation in 3D space may be represented by a matrix product between the points x and the rotation matrix R . The translation, however, will be calculated as the sum vector of the points x and the translation vector t . So it will be assumed that the reference surface which is to be transformed with the function:

$$\tau(X_i^{source}) = RX_i^{source} + t \quad (\text{A.2})$$

It calculates the difference between the target and the reference, after the transformation:

$$x_i^{target} - \tau(x_i^{target}) = x_i^{target} - (R(x_i)^{source} + t) \quad (\text{A.3})$$

Finally, for the whole cloud points, we can calculate the total error in this way:

$$\operatorname{argmin}_{R,t} = \frac{1}{N} \sum_{i=0}^n (x_i)^{\operatorname{target}} - (Rx_i^{\operatorname{source}} + t) \quad (\text{A.4})$$

Bibliography

- [1] A. Holton, E. Walsh, A. A. G. P. and R. Venugopalan (2002). Comparative mri compatibility of 316l stainless steel alloy and nickel-titanium alloy stents. *Journal of Cardiovascular Magnetic Resonance* 4, 423–430.
- [2] Andreasen, G. F. and T. B. Hilleman (1971). An evaluation of 55 cobalt substituted nitinol wire for use in orthodontics. *The Journal of the American Dental Association* 82, 1373–1375.
- [3] A.R Pelton, J. Fino-Decker, L. V. C. B. P. S. M. L. M. M. (2013). Rotary-bending fatigue characteristics of medical-grade nitinol wire. *Journal oh the mechanical behavior of biomedical materials* 27 (2013) 27, 19–32.
- [4] Asch, M. R. (2002). Initial experience in humans with a new retrievable inferior vena cava filter. *Radiology* 225, 835–844.
- [5] Azaouzi, M., A. Makradi, and S. Belouettar (2012). Deployment of a self-expanding stent inside an artery: A finite element analysis. *Materials and Design* 41, 410–420.
- [6] C. Kleinstreuer, Z. Li, C. B. S. S. M. F. (2008). Computational mechanics of nitinol stent grafts. *Journal of Biomechanics* 41, 2370–2378.
- [7] Cattaneo, M. (2006). *Caratterizzazione biomeccanica sperimentale di stent-grafts*. Tesi di Laurea, Politecnico di Milano.
- [8] Coats, L. and P. Bonhoeffer (2007). New percutaneous treatments for valve disease. *Heart* 93, 639–644.
- [9] D. J. Hoh, B. L. Hoh, A. P. A. and M. Y. Wang (2009). Shape memory alloys: metallurgy, biocompatibility, and biomechanics for neurosurgical applications. *Neurosurgery* 64, 199–214.
- [10] F. Auricchio, M. Conti, M. D. B. G. d. S. (2011). Carotid artery stenting simulation: from patient-specific images to finite element analysis. *Med. Eng. Phys.* 33, 281–289.

- [11] F. Auricchio, R. T. (1996). Shape-memory alloys: modeling and numerical simulations of the finite-strain superelastic behavior, *comput.meth.appl. Journal of the mechanical behavior of biomedical materials* 143, 175–194.
- [12] F. Auricchio, M.Conti, S. M. A. R. J. S. (2013). Patient-specific aortic endografting simulation :from diagnosis to prediction. *Computers in Biology and Medicine* 43, 386–394.
- [13] Giuseppe C. Balboni, e. a. (Ristampa 2000). *Anatomia Umana*. Edi. Ermes s.r.l.
- [14] J. A. Kaufman, S. C. Geller, D. C. B. e. a. (2000). Endovascular repair of abdominal aortic aneurysms: current status and future directions. *American Journal of Roentgenology* 175, 289–302.
- [15] K. R. Dai, X. K. Hou, Y. H. S. R. G. T. S. J. Q. and C.Ni (1993). Treatment of intra-articular fractures with shapememory compression staples. *Injury* 24, 651–655.
- [16] Lagoudas, D. C. (2008). *Shape Memory Alloys: Modeling and Engineering Applications*. Springer.
- [17] Lipscomb, I. P. and L. D. M. Nokes (1996). The application of shape memory alloys in medicine. *Paston Press Ltd, Norfolk, Va, USA*,.
- [18] Marconi, S. (2010-2011). *Ricostruzione 3D virtuale e fisica del pancreas con discriminazione semiautomatica tra parenchima sano e tessuto tumorale*. Ph. D. thesis, Corso di Laurea Specialistica in Ingegneria Biomedica.
- [19] Migliavacca, F., L. Petrini, M. Colombo, and F. Auricchio (2002). Mechanical behavior of coronary stents investigated through the finite element method. *Journal of Biomechanics* 35, 803–811.
- [20] Otsuka, K. . W. (1998). *Shape Memory Materials*. Cambridge University Press.
- [21] Paul A. Yushkevich, Joseph Piven, H. C. H. R. G. S. S. H. J. C. G. and G. Gerig. (2006). User-guided 3d active contour segmentation of anatomical structures: Significantly improved efficiency and reliability. *Neuroimage* 31 (3), 1116–28.
- [22] Petrini, L. and F. Migliavacca (2011). Biomedical applications of shape memory alloys. *Journal of Metallurgy* 2011.
- [23] Rebelo, N., R. Radford, A. Zipse, M. Schlun, and G. Dreher (2011). On modeling assumptions in finite element analysis of stents. *Journal of medical devices* 5.

- [24] Ryhanen, J. (1999). Biocompatibility evaluation of nickel-titanium shape-memory metal alloy. *Ph.D. dissertation, University of Oulu, Department of Surgery, Oulu, Finlandia,*.
- [25] S. De Bock, F. Iannaccone, G. D. S. (2012). Virtual evaluation of stent graft deployment: A validated modeling and simulation study. *Journal of the machanical behavior of biomedical materials* 13, 129–139.
- [26] Shabalovskaya, S. A. (1996). On the nature of the biocompatibility and on medical applications of niti shape memory and superelastic alloys. *Bio-Medical Materials and Engineering* 6, 267–289.
- [27] T. W. Duerig, K. N. P. and D. Stockel (1997). Superelastic nitinol for medical devices. *Medical Plastics and Biomaterials* 2, 30–43.
- [28] Xiao-Yan Gong, Alan R. Pelton, T. W. D. N. R. and K. Perry (2003). Finite element analysis and experimental evaluation of superelastic nitinol stents. *Journal oh the mechanical behavior of biomedical materials*.